Astronomy & Astrophysics manuscript no. main_GCPair
June 28, 2021
©ESO 2021

arXiv:submit/3813297 [astro-ph.CO] 28 Jun 2021

The *eROSITA* view of the Abell 3391/95 field: a case study from the Magneticum cosmological simulation

Veronica Biffi[1,2,3⋆], Klaus Dolag[1], Thomas H. Reiprich[4], Angie Veronica[4], Miriam E. Ramos-Ceja[5], Esra Bulbul[5], Naomi Ota[4,6], and Vittorio Ghirardini[5]

[1] Universitaets-Sternwarte Muenchen, Ludwig-Maximilians-Universität München, Scheinerstr. 1, D-81679 Munich, Germany
[2] INAF - Osservatorio Astronomico di Trieste, via Tiepolo 11, I-34143 Trieste, Italy
[3] IFPU - Institute for Fundamental Physics of the Universe, Via Beirut 2, I-34014 Trieste, Italy
[4] Argelander-Institut für Astronomie (AIfA), Universität Bonn, Auf dem Hügel 71, 53121 Bonn, Germany
[5] Max-Planck-Institut für extraterrestrische Physik, Gießenbachstraße 1, D-85748 Garching, Germany
[6] Department of Physics, Nara Women's University, Kitauoyanishi-machi, Nara, 630-8506, Japan

Received ; accepted

ABSTRACT

Context. Clusters of galaxies reside at the nodes of the Cosmic Web, interconnected by filamentary structures that contain tenuous diffuse gas, especially in the warm-hot phase. Galaxy clusters grow by merging of smaller objects and gas, mainly accreted through these large-scale filaments. For the first time, the large-scale cosmic structure and a long gas emission filament have been captured by SRG/*eROSITA* in a direct X-ray observation of the A3391/95 field.

Aims. We aim at investigating the assembly history of an A3391/95-like system of clusters and the thermo-chemical properties of the diffuse gas in it, connecting simulation predictions to the *eROSITA* observations, to constrain the origin and nature of the gas in the pair interconnecting bridge.

Methods. We analysed the properties of a system resembling A3391/95, extracted from the $(352\,h^{-1}\,\mathrm{cMpc})^3$ volume of the Magneticum Pathfinder cosmological simulations at $z = 0.07$. We tracked back in time the main progenitors of the pair clusters and of surrounding groups to study the assembly history of the system and its evolution.

Results. Similarly to the observed A3391/95 system, the simulated cluster pair is embedded in a complex network of gas filaments, with structures aligned over more than 20 projected Mpc and the whole region collapsing towards the central overdense node. The spheres of influence ($3 \times R_{200}$) of the two main clusters already overlap at $z = 0.07$, but their virial boundaries are still physically separated. The diffuse gas located in the interconnecting bridge closely reflects the WHIM, with typical temperature of ~ 1 keV and overdensity $\delta \sim 100$, with respect to the mean baryon density of the Universe, and lower enrichment level compared to the ICM in clusters. We find that most of the bridge gas collapsed from directions roughly orthogonal to the intra-cluster gas accretion directions, and its origin is mostly unrelated to the two cluster progenitors. We find clear signatures in the surrounding groups of infall motion towards the pair, such as significant radial velocities and slowdown of gas compared to dark matter. These findings further support the picture of the Northern Clump (MCXC J0621.7-5242) cluster infalling along a cosmic gas filament towards Abell 3391, possibly merging with it.

Conclusions. We conclude that, in such a configuration, the pair clusters of the A3391/95-like system are in a pre-merger phase, and did not interact yet. The diffuse gas in the interconnecting bridge is mostly warm filament gas, rather than tidally-stripped cluster gas.

Key words. X-rays: galaxies: clusters – Galaxies: clusters: intracluster medium

1. Introduction

The formation and evolution of the large scale structure (LSS) has long been a key target of astrophysical and cosmological investigations. Simulations predict the existence of a thin filamentary structure, the so-called Cosmic Web (Bond et al. 1996), connecting the knots where galaxy clusters reside. Observationally, a detailed study of the Cosmic Web structure and evolution can be pursued by investigating the properties of the visible matter tracing the underlying dark matter (DM) distribution. This promoted several investigations aiming for a census of cosmic baryons (Persic & Salucci 1992; Fukugita et al. 1998). Compared to observational estimates, theoretical studies predict that about half of the baryons in the Universe must be indeed undetected (Cen & Ostriker 1999; Davé et al. 2001). In particular, independently of the use of identification tools used to identify the Cosmic Web constituents (e.g. Libeskind et al. 2018) — namely filaments, sheets and voids — cosmological simulations consistently predict that a significant fraction ($\sim 40\%$) of the cosmic baryon budget is in the form of cool intergalactic medium and warm-hot intergalactic medium (WHIM, Cui et al. 2019; Martizzi et al. 2019), with most of it located in filaments (Tuominen et al. 2020). Properties of cosmic filament populations have also been studied from a statistical point of view, in order to characterize their evolution and global properties in correlation with their tracers, namely gas and galaxies (Gheller et al. 2015, 2016; Cui et al. 2018; Martizzi et al. 2019). Recent investigations of various state-of-the-art cosmological simulations, including the Magneticum Pathfinder suite analysed in the present study, show that statistically different populations exist: longer thinner filaments typically connecting smaller structures, and shorter bridge-like filaments usually denser and connected to massive objects (Galárraga-Espinosa et al. 2020a,b).

⋆ e-mail: veronica.biffi@inaf.it, biffi@usm.lmu.de

Observational reconstructions of the Cosmic Web are therefore tightly connected to the extensive search for the diffuse cold gas and WHIM in the filaments, which is still largely eluding our detections (Bregman 2007). Reconstructions of the LSS through galaxy mapping have been successfully performed over the last decades (see, e.g., Tempel et al. 2014; Malavasi et al. 2020). For what concerns the gaseous content of the LSS, observations have been carried out mainly in the far-UV (see Bregman 2007; Péroux & Howk 2020, for a review), whereas, in the X rays, direct observations of the gaseous Cosmic Web has proven to be very challenging (Nicastro et al. 2008). The main reason for this lies in the difficulty of observing the tenuous warm plasma residing in the filaments, whose low densities ($< 10^{-4}$ cm^{-3}) and temperatures ($T \sim 10^5$–10^7 K) make its X-ray emission very faint. Only recently significant progresses have been done in this direction, starting with the first detection of the WHIM reported by Nicastro et al. (2018), obtained from the absorption lines of highly ionized oxygen (OVII) in high signal-to-noise spectra of a quasar at $z > 0.4$, using the XMM-Newton Reflection Grating Spectrometer (RGS). Overall, direct observations of warm gas in filaments have been mainly limited to special cases, such as specific lines of sight in the direction of high-redshift quasars for the detection of WHIM in intervening absorbers (Nevalainen et al. 2015; Nicastro et al. 2018; Nevalainen et al. 2019; Kovács et al. 2019) or regions in between close pairs of clusters or close to cluster outskirts where the WHIM emission could be enhanced (e.g. Briel & Henry 1995; Finoguenov et al. 2003; Durret et al. 2004). Longer gaseous filamentary structures, up to tens of h^{-1} cMpc, have been instead investigated mostly through statistical approaches, such as stacking of thermal-SZ and X-ray observations (de Graaff et al. 2019; Tanimura et al. 2020a,b; Lim et al. 2020). Recently, Khabibullin & Churazov (2019) investigated the potential of *eROSITA* stacking approaches in characterising the WHIM. Specifically, accounting for the contribution of the resonantly scattered cosmic X-ray background and comparing the WHIM imprints in X-ray absorption and emission, they show that truly diffuse gas, filling cosmic filaments, can be significantly characterised and better differentiated from denser matter clumps.

A promising strategy for direct detections of the WHIM X-ray emission is focusing on specific regions encompassing multiple cluster systems (like merging clusters and superclusters) or on the prolongation of cluster outskirts (Fujita et al. 2008; Planck Collaboration et al. 2013; Eckert et al. 2015; Bulbul et al. 2016; Hattori et al. 2017; Akamatsu et al. 2017; Parekh et al. 2017; Connor et al. 2018, 2019; Ghirardini et al. 2020). In fact, a number of cluster binary systems in the local Universe have been throughly investigated to find evidences for the presence of cosmic diffuse gas in the bridges connecting the member clusters. Well known case studies in the low-redshift Universe are represented by A3556 and A3558 in the Shapley supercluster ($z = 0.048$, Mitsuishi et al. 2012; Ursino et al. 2015); RXC J1825.3+3026 ($z \sim 0.065$) and CIZA J1824.1+3029 ($z \sim 0.071$; Botteon et al. 2019); the A399–A401 system (at redshifts $z \sim 0.0724$ and $z \sim 0.0737$, respectively Sakelliou & Ponman 2004; Fujita et al. 2008; see also thermal SZ observations by Bonjean et al. 2018); the merging pair A222–A223 ($z \sim 0.21$; Werner et al. 2008), or the multiple merging system Abell 1758 ($z \sim 0.28$; Durret et al. 2011).

Among these, also the cluster system A3391–A3395 has been widely studied in the literature, with special attention to the gaseous bridge between the pair members (Tittley & Henriksen 2001). This system comprises two main clusters, the northern one, Abell 3391, and the southern one, Abell 3395 (a double system itself; Reiprich & Böhringer 2002) at $z \sim 0.05$, separated by about 50′ (approximately 3 Mpc) on the sky. Both systems have X-ray temperatures around $T_X \sim 5$ keV (Reiprich & Böhringer 2002; Vikhlinin et al. 2009). Early results by Reiprich & Böhringer (2002), combining *ROSAT* and *ASCA* data, indicated masses of $M_{500} \sim 5 \times 10^{14}M_\odot$ for A3391 and $M_{500} \sim 8.8 \times 10^{14}M_\odot$ for both A3395s and A3395n (assuming an Einstein–de Sitter cosmology and a Hubble constant $H_0 = 50$ km s^{-1}Mpc^{-1}). Especially for A3395, and despite the uncertainties, these values were likely overestimated, probably due to the merging phase of the system. More recent estimates by Piffaretti et al. (2011), based on *ROSAT* X-ray luminosities, report lower masses of about $M_{500} \sim 2 \times 10^{14}M_\odot$ for both A3391 and A3395.

From previous studies, debated conclusions have been drawn on the dynamical status of the pair, with different interpretations of the nature of the gas observed between the two main clusters (Tittley & Henriksen 2001; Planck Collaboration et al. 2013; Sugawara et al. 2017; Alvarez et al. 2018). Sugawara et al. (2017) and Alvarez et al. (2018), for instance, report the presence of hot gas in the bridge region, concluding that this could have been tidally stripped or heated by the interaction between A3391 and A3395. This is in contrast with earlier *ASCA* and *ROSAT* results from Tittley & Henriksen (2001), rather favouring a scenario in which the filament connecting the two systems is in fact longer and aligned lengthwise with the line of sight (l.o.s.). The geometry of the system with respect to the l.o.s. and the temperature of the interconnecting gas are key aspects to interpret the nature of the bridge, where the detection of cold-warm gas with $T \lesssim 1$ keV can indicate the presence of true filament gas.

More recently, the A3391/95 system has also been targeted by the German-built X-ray telescope on board the Spectrum-Roentgen-Gamma (SRG) mission, the extended ROentgen Survey with an Imaging Telescope Array (*eROSITA*; Predehl et al. 2020), during the Performance Verification (PV) phase observational campaign (Reiprich et al. 2021). Thanks to the high sensitivity in the soft X-ray band, large field of view and good spatial resolution (Merloni et al. 2012), these *eROSITA* observations allowed to find hints of emission from warm gas in the pair bridge, in addition to the known hotter gas emission. In the *eROSITA* observation, the bridge emission qualitatively spans ~ 3 Mpc (projected) (Reiprich et al. 2021), which cannot be entirely attributed to the known galaxy group (ESO 161-IG 006) located in between the two main clusters. Furthermore, the emission from hot and warm diffuse gas is detected well beyond the projected virial boundaries of the main clusters, allowing for the first time to map a continuous warm-hot emission filament in the X rays, spanning from north to south 4 degrees across the observed field. This WHIM filament extends north of A3391 and south of A3395 for a total projected length of ~ 15 Mpc, at the median redshift of the system, and its presence is confirmed through the Planck SZ map and DECam (optical) galaxy density distribution as well. With this unprecedented X-ray detection of a WHIM filament in the observation of a single system reported by Reiprich et al. (2021), the new *eROSITA* PV observations are also capturing the formation of the LSS in the region where the system is located. In fact, several groups and clusters are discovered in its local environment (i.e. at the same redshift) and there are indications of the substructures moving towards the A3391/95 system (see Veronica et al., submitted; Ramos-Ceja et al., in prep.).

With the primary goal of accompanying the observational results obtained by the *eROSITA* PV observations of the Abell 3391/95 system and its surroundings, and help their interpretation, we resort here to cosmological hydrodynamical simula-

tions. Specifically, we focus on a simulated pair of galaxy clusters extracted from the Magneticum cosmological hydrodynamical simulation, sharing several similarities with the observed A3391/95 system. The simulated analog allows us to investigate the intrinsic properties of an A3391/95-like system and its formation and evolution. In particular, we aim at reconstructing the system assembly history considering the main clusters and the additional structures in the surrounding environment. Furthermore, we can make use of the simulations to study the thermal and chemical properties of the diffuse gas component in the system, both at the selection redshift ($z = 0.07$) and throughout the cosmic evolution. This will allow us to explore the expected properties of the WHIM and of the bridge gas, and to compare them against the ICM characteristics within the clusters. Especially, we can directly investigate the origins of the gas in the region between the pair clusters, to determine whether this can be filament gas or rather tidally-stripped intracluster gas.

The paper is organized as follows. In Sec. 2 we present the simulation suite used for the present analysis, namely the Magneticum Pathfinder cosmological hydrodynamical simulations. Interested in multiple cluster systems in the local Universe, we focus on one simulation snapshot at low redshift ($z = 0.07$) and explore in Sec. 3 the cluster pair candidates available, depending on three-dimensional and projected separation, as well as on the mass and mass ratio of the members. Among those, we select and introduce the best cluster pair selected to represent the theoretical analog of the observed A3391/95 system (Sec. 3.1). In Sec. 4 we illustrate the main results of our study. The three-dimensional assembly of the pair system in the Cosmic Web, with its local evironment, is presented in Sec. 4.1 together with the results on the origin of the diffuse gas residing in the bridge between the pair member clusters. In Secs. 4.2 and 4.3 we discuss instead the thermal and chemical properties, and their time evolution, of the diffuse gas in various thermal phases and spatial regions in and around the pair. In Sec. 4.4 we then investigate the groups aligned along large-scale filaments connected to the pair, in order to find the signatures of their infall towards the overdense Cosmic Web knot where the pair is located. Finally, we summarize and conclude in Sec. 6.

2. Magneticum Pathfinder Simulations

We employ a large cosmological volume, simulated including a variety of physical processes, to study the properties of multiple galaxy cluster systems and the evolution of the local Cosmic Web in which they are embedded.

To this scope, we consider the Magneticum Pathfinder simulations[1], a set of state-of-the-art cosmological smoothed-particle hydrodynamics (SPH) simulations, comprising boxes of different volumes and resolution. The simulations have been performed with the TreePM/SPH code P-Gadget3, an extended version of P-Gadget2 (Springel 2005). This includes several improvements of the SPH formulation, such as the treatment of viscosity and artificial conduction, and the use of higher-order kernels (Dolag et al. 2005; Beck et al. 2016). The code also accounts for a large variety of physical processes describing the evolution of the baryonic components. These comprise radiative cooling and heating from a uniform time-dependent ultraviolet (UV) background (Haardt & Madau 2001), as well as a sub-resolution model for star formation (Springel & Hernquist 2003). Following detailed stellar evolution models, a description of chemical enrichment is also included as in Tornatore et al. (2004, 2007). Specifically, metals are produced from stellar sources depending on their mass and typical lifetimes, assuming an initial mass function (IMF) according to Chabrier (2003) and a mass-dependent lifetime function from Padovani & Matteucci (1993). The three main enrichment channels are supernovae Type Ia (SNIa) and Type II (SNII) and low- and intermediate-mass stars undergoing the Asymptotic Giant Branch (AGB) phase. Eleven different chemical elements are explicitely traced (namely, H, He, C, Ca, O, N, Ne, Mg, S, Si, and Fe) assuming stellar yields from van den Hoek & Groenewegen (1997), for AGB stars, Thielemann et al. (2003) for SNIa and Woosley & Weaver (1995) for SNII. Gas radiative cooling depends on the local gas metallicity in a self-consistent way, as described in Wiersma et al. (2009). SNII also contribute to thermal and kinetic energy feedback by driving galactic winds, with a mass loading rate proportional to the star formation rate (SFR) and a resulting wind velocity of $v_w = 350\,\mathrm{km\,s^{-1}}$ (Springel & Hernquist 2003). The simulations further account for black hole (BH) growth and gas accretion, powering energy feedback from Active Galactic Nuclei (AGN), based on the implementation by Springel et al. (2005) and Di Matteo et al. (2005) and with modifications as in Fabjan et al. (2010). As shown in previous studies, the Magneticum simulations successfully reproduce many observed properties of cosmic structures, such as kinematical and morphological properties of galaxies (Teklu et al. 2017; Remus et al. 2017; Schulze et al. 2018; Remus & Forbes 2021), chemical properties of both galaxies and clusters (Dolag et al. 2017), statistical properties of the AGN population at various redshifts (Hirschmann et al. 2014; Steinborn et al. 2016; Biffi et al. 2018a). At cluster scales, the Magneticum set has been employed to constrain the scatter in the observable X-ray luminosity-temperature relation via intracluster medium (ICM) velocity diagnostics (Biffi et al. 2013) as well as the pressure profile of the ICM (Gupta et al. 2017), and to explore the level of contamination of ICM emission due to the central AGN, expected for synthetic *eROSITA* observations (Biffi et al. 2018a).

Given the number of well known observed cluster pairs at low redshift, and motivated in particular by the *eROSITA* PV observation of the A3391–A3395 system, we focus on the simulation snapshot corresponding to redshift $z = 0.07$. The specific simulation considered is one of the larger ones, namely the Magneticum "Box2" cosmological box at high resolution ("hr"). This box comprises a comoving volume of $(352\,h^{-1}\,\mathrm{cMpc})^3$ and is resolved with 2×1584^3 particles, corresponding to a mass resolution of $m_{\mathrm{DM}} = 6.9 \times 10^8\,h^{-1}\,\mathrm{M}_\odot$ and $m_{\mathrm{gas}} = 1.4 \times 10^8\,h^{-1}\,\mathrm{M}_\odot$, for dark matter and gas particles respectively (see also Biffi et al. 2018a). Since the gas can spawn up to four stellar particles decreasing its mass, or accrete metals from chemical pollution, the mass of the gas particles can vary in time. At this resolution, the softening length for DM and gas particles is $\epsilon_{\mathrm{DM,gas}} = 3.75\,h^{-1}\,\mathrm{kpc}$ and for stellar particles $\epsilon_{\mathrm{stars}} = 2\,h^{-1}\,\mathrm{kpc}$. The simulations assume a standard ΛCDM cosmological model with the Hubble parameter set to $h = 0.704$, the density parameters for matter, dark energy and baryons equal to $\Omega_M = 0.272$, $\Omega_\Lambda = 0.728$ and $\Omega_b = 0.0451$, and $\sigma_8 = 0.809$, for the normalization of the fluctuation amplitude at 8 Mpc (according to the seven-year results of the Wilkinson Microwave Anisotropy Probe, WMAP, Komatsu et al. 2011). The data of the simulation volume used for the present analysis, with several precomputed halo properties and mock X-ray data (generated with the PHOX X-ray photon simulator, Biffi et al. 2012, 2013), are

[1] www.magneticum.org

publicly available on the Cosmological Web Portal[2] (Ragagnin et al. 2017).

In order to identify subhalos, we employ the SUBFIND substructure finding algorithm (Springel et al. 2001; Dolag et al. 2009). The main halo detection is based on a standard friends-of-friends algorithm (FoF; Davis et al. 1985). Taking into account the presence of baryons as well (Dolag et al. 2009), SUBFIND also identifies all self-bound substructures within main halos, around local density peaks. In particular, the subhalos of a cluster are defined as all the substructures identified within its virial radius ($R_{\rm vir}$, computed with the spherical-overdensity approach using the top-hat model by Eke et al. 1996). SUBFIND also allows to identify for each substructure the corresponding content of gravitationally bound DM, gas, stars etc. The center of each halo is identified with the position of the minimum of the potential well, considering the member particles.

For each main structure, characteristic quantities are computed, such as characteristic radii and enclosed masses. For data comparison purposes, we compute the R_{500} radius, i.e. the radius of the sphere encompassing an average density that is 500 times the critical density of the Universe ($\rho_{\rm cr}$), and the mass within it, M_{500}. The estimate of R_{200} used in the following corresponds for simplicity to $1.5 \times R_{500}$, and we verified that this matches within a few percents the value computed at the actual overdensity of $\Delta = 200$.

For all metallicity values reported in this work, we refer for simplicity to the solar abundance pattern by Anders & Grevesse (1989) as a reference. Given that the solar unit is purely used to normalize our estimates, this can be easily re-scaled for other solar reference values, such as Asplund et al. 2009[3].

3. Galaxy cluster pair candidates

In the Magneticum "Box2/hr" box at $z = 0.07$, there are a total of 10429 identified haloes with masses in the range $10^{13} < M_{500}[{\rm M}_\odot] < 1.44 \times 10^{15}$. In particular, we identify 448 objects with $M_{500} > 10^{14}\,{\rm M}_\odot$, from which we can therefore expect $\sim 10^5$ candidate pairs of individually-identified cluster-size haloes.

Motivated by the properties of observed pairs of galaxy clusters, for which a variety of observations have been dedicated to investigating their properties, the stage of interaction and the possible detection of filamentary structures (bridges) physically connecting them, we further restrict the search to the "close" pairs, in projection. We find that only 535(135) pairs appear closer than 10(5) Mpc in at least one projection (considering the three Cartesian axes x, y and z as possible l.o.s. directions). By inspecting the three-dimensional spatial distribution of all the cluster-size haloes in the simulated volume, we find nevertheless that only for 146, 88 and 40 unique pairs the 3D distance between the two haloes is actually smaller than 20, 15 and 10 megaparsecs, respectively (see Table A.1, in Appendix A). The number of close pairs decreases further if we impose additional constraints on the mass ratio between the two haloes, or on the initial mass-range selection of the clusters. We see in particular that for haloes with masses comprised in the range $1.5\text{–}3.5 \times 10^{14}\,{\rm M}_\odot$, only 25 candidate pairs are in fact closer than $d_{\rm 3D} < 20$ Mpc, with $\sim 30\%$ of them actually closer than $d_{\rm 3D} < 10$ Mpc.

[2] https://c2papcosmosim.uc.lrz.de

[3] For instance, in order to adopt the Asplund et al. 2009 solar pattern instead of Anders & Grevesse (1989), the Fe abundances reported in the following Sections should be multiplied by a factor $Z^{\rm AG89}_{\rm Fe,\odot}/Z^{\rm Aspl09}_{\rm Fe,\odot} = 4.68 \times 10^{-5}/3.16 \times 10^{-5} \sim 1.5$

These results for Box2/hr at $z = 0.07$ indicate that we expect roughly ~ 400 pairs per Gpc^3 with cluster size members ($M_{500} > 10^{14}{\rm M}_\odot$) separated by a physical distance smaller than 10 Mpc. In most of the cases ($\sim 70\%$) the mass ratio of the member clusters does not exceed 2, and in 20% of them the members have in fact comparable masses (M1/M2 $\sim$ 1). In order to confirm this, we investigated also larger cosmological volumes (namely boxes with $0.9\,h^{-1}$ cGpc and $2.7\,h^{-1}$ cGpc per side) at similar resolution, that are part of the Magneticum simulation set. In the local Universe ($z \sim 0$), we consistently find ~ 300 cluster pairs per Gpc^3 volume with three-dimensional separation lower than 10 Mpc and member masses $M_{500} > 10^{14}{\rm M}_\odot$. By restricting to member clusters with $1.5 < M^{1,2}_{500}\,[10^{14}\,{\rm M}_\odot] < 3.5$, we expect to find ~ 50 close ($d_{\rm 3D} \lesssim 10$ Mpc) pairs per Gpc^3 — with 50% of them having a mass-ratio M1/M2 $\lesssim$ 1.2–1.3.

In order to compare against the specific case of A3391/95, we choose one of the 7 close pairs at $z = 0.07$ (member separation of $d_{\rm 3D} < 10$ Mpc and mass ratio $1 <$ M1/M2 $\lesssim 1.2$) for deeper investigation, as a study case in the simulations that fairly resembles the observed A3391–A3395 system. The specific selection has been performed based on a visual inspection of each candidate, taking into consideration also the projected distances between the member clusters in the three main projections of the simulation box (namely, we restrict for simplicity to those along the x, y and z Cartesian axes). We remark nonetheless that each candidate among those with similar member masses, mass ratio and physical separation could have been in principle chosen, by inspecting among all the possible l.o.s. the projection which resembles as close as possible the observed system.

3.1. A3391–A3395: a simulation analog

The close galaxy cluster pair, selected at $z = 0.07$ as a case study, comprises two haloes with masses $M^1_{500} = 1.96 \times 10^{14}\,{\rm M}_\odot$ (GC1) and $M^2_{500} = 1.67 \times 10^{14}\,{\rm M}_\odot$ (GC2), respectively, namely with a mass ratio of ~ 1.17. The two pair members are physically separated by $d_{\rm 3D} = 4.54$ Mpc and the projected distance is 2.6, 4.5 and 3.8 megaparsecs in the xy, xz and yz projection planes, respectively. The physical distance between their centers corresponds roughly to three times the sum of their R_{500} radii, respectively $R^1_{500} = 862$ kpc and $R^2_{500} = 819$ kpc. This is equivalent to $d_{\rm 3D} \sim 2 \times (R^1_{200} + R^2_{200})$, considering $R_{200} \approx 1.5 \times R_{500}$. The top-hat virial radii, $R_{\rm vir}$, are similar and both approximately 50% larger than R_{200} (namely, $R^1_{\rm vir} = 1.88$ Mpc and $R^2_{\rm vir} = 1.87$ Mpc). The spheres approximating $3 \times R_{200}$ are therefore already overlapping, physically and, therefore, also in projection.

We select this pair, in particular, in the reference xy projection (i.e. with the l.o.s. along the z-axis of the cosmological box), motivated by the similarities with the A3391–A3395 system — as shown in Fig. 1. In the central panel of the Figure, we report the *eROSITA* PV observation of the $\sim 15\,{\rm deg}^2$ region around A3391/95 (Reiprich et al. 2021), with all the main systems labelled. In the right panel of Fig. 1 we report the gas density map of the simulated analog at $z = 0.07$, comprising a cubic volume of $20\,h^{-1}$ cMpc per side. Compared to the observed system, the GC1 and GC2 clusters have a broadly similar orientation, and are surrounded by other systems aligned in a filamentary structure from top to bottom over $20\,h^{-1}$ cMpc in projection (approximately 26 physical Mpc at this redshift). Fig. 1-left shows a simulation zoom onto the central $10\,h^{-1}$ cMpc-size region, roughly covering the same size of the eROSITA field. Here we label the two main clusters and their sizes, an infalling group-size halo (see Sec. 4.4), and mark in blue the interconnecting gas bridge.

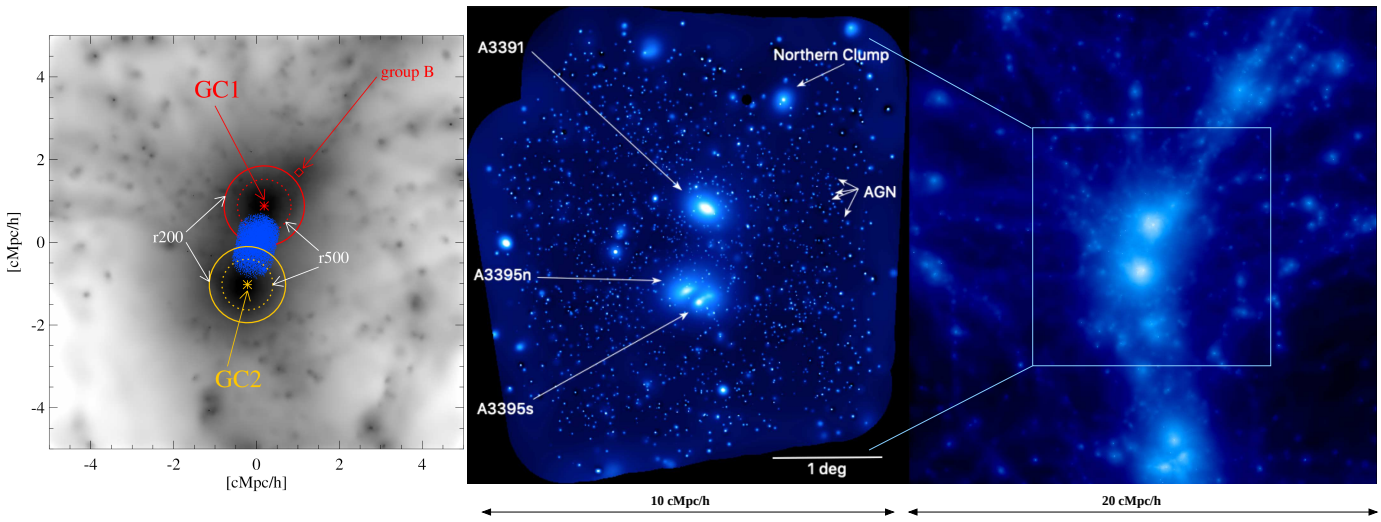

Fig. 1: Comparison between the simulated galaxy pair candidate at $z = 0.07$ and the observed A3391/95 system. *Left:* zoom onto the projected gas density map of the simulated cluster pair. The image is $10\,h^{-1}$ cMpc per side and projected for $10\,h^{-1}$ cMpc along the l.o.s. We label the two clusters GC1 and GC2 and an infalling group ("group B"), and mark their extent. In blue, is shown the gas in the interconnecting bridge. *Middle: eROSITA* PV observation of a $\sim 15\,\mathrm{deg}^2$ region around the multiple A3391/95 system, with the main clusters and Northern Clump marked (Reiprich et al. 2021). Here, 1 deg ≈ 3.9 Mpc, at the redshift of A3391 and for the cosmology adopted in Reiprich et al. (2021) (for comparison to simulations, we also report the comoving scale). *Right:* projected gas density map of the simulated cluster pair in its local environment. The map encloses a $(20\,h^{-1}\,\mathrm{cMpc})^3$ volume, spanning ~ 26 Mpc (physical) in projection, for the chosen redshift and cosmology.

On the plane of the sky, they appear to be at a relatively similar distance (~ 3 Mpc) compared to the observed A3391/95, in which the projected $3 \times R_{200}$ extent of the two main systems also overlap.

Compared to the simulations, the mass of the observed A3391/95 system reported by Piffaretti et al. (2011) is similar, although $\sim 25\%$ more massive overall, with $M_{500} = 2.16{\times}10^{14}\,\mathrm{M}_\odot$ and $M_{500} = 2.4 \times 10^{14}\,\mathrm{M}_\odot$ for A3391 and A3395, respectively (Piffaretti et al. 2011; Alvarez et al. 2018). Similarly to those works, for the purpose of comparing to simulations, we will mainly consider the A3391/95 system as a cluster pair, treating A3395 as a whole although it is a double-peaked merging cluster Reiprich & Böhringer (2002); Reiprich et al. (2021). We note nonetheless that the southern GC2 cluster in the simulations shows a broad similarity with A3395, hosting two massive substructures that recently merged (see further discussion in Sec. 5).

In Fig. 2 we show the evolution of the system in its local environment from $z = 1$ down to $z = 0.07$ (from left to right). The maps show the gas surface density (upper row) and ideal X-ray emission in the [0.5–2] keV band (lower row) at three representative redshifts $z = 1.04$, $z = 0.47$ and $z = 0.07$, projected along the z-axis and centered on the pair center of mass. In order to visualize the local environment around the system, these maps comprise a comoving volume of $(20\,h^{-1}\,\mathrm{cMpc})^3$. Overdense and higher-emission regions are marked with lighter colors in the top panels and blue-magenta colors in the bottom ones.

The evolution of this region shows how the assembly of structures proceeds along filaments, by the accretion and merging of smaller structures and diffuse matter. From the X-ray emission (Fig. 2, lower panels), one can notice that the main systems are aligned along a top-down direction, and the two pair members are enclosed by a common higher-emissivity envelope, tracing the X-ray emitting diffuse gas. From the left-most panel, we see that at $z \sim 1$ the cores of the main cluster progenitors are already distinguishable, as well as the other main haloes in the surroundings. Compared to the gas density maps, this allows us to better single out the principal filamentary structure defined by the main massive structures aligning in the field and embedded in the diffuse gaseous component. In fact, minor gas filaments that are visible in the density maps are too faint to significantly emit in the X-ray, even when the soft band is considered. The X-ray maps in Fig. 2 indicate a remarkable resemblance with the *eROSITA* PV observations of the A3391/95 field, where a $\sim$ 15 Mpc gas emission filament has been detected thanks to *eROSITA* large FoV ($\sim$ 1 deg) and superior soft X-ray effective area. The observed filamentary gas emission extends north and south from the A3391/95 system spanning $\sim$ 4 degrees in the sky and connecting other extended structures, namely groups and clusters, all at the same redshift (Reiprich et al. 2021).

3.1.1. Gas bridge between the pair clusters.

A debated aspect of the observed A3391/95 system regards the nature of the gas between the two main clusters. Following the common terminology, the gas filament between clusters in close pairs is typically referred to as "bridge". Depending on the interaction stage of the two systems, this could be either stripped gas from the outer cluster atmospheres or actual filament gas.

Distinguishing pure filament gas from outer cluster atmospheres is *per se* very challenging, in observations but also in simulations. Therefore, it is difficult to define the exact boundaries of the bridge. In our simulations, we define the interconnecting bridge as a three-dimensional cylinder-like volume in between the two main clusters. For simplicity, we define the bridge main axis as the three-dimensional line connecting the centers of GC1 and GC2. For the radius of the cylinder, we assume ~ 660 kpc. Along the main axis, the bridge is limited to the region outside of R_{200} of each cluster. Given the physical separation of the two clusters, this corresponds to ~ 2 Mpc along the spine direction. We verified that either taking a right cylinder (with flat ends) or modifying the main axis direction to account

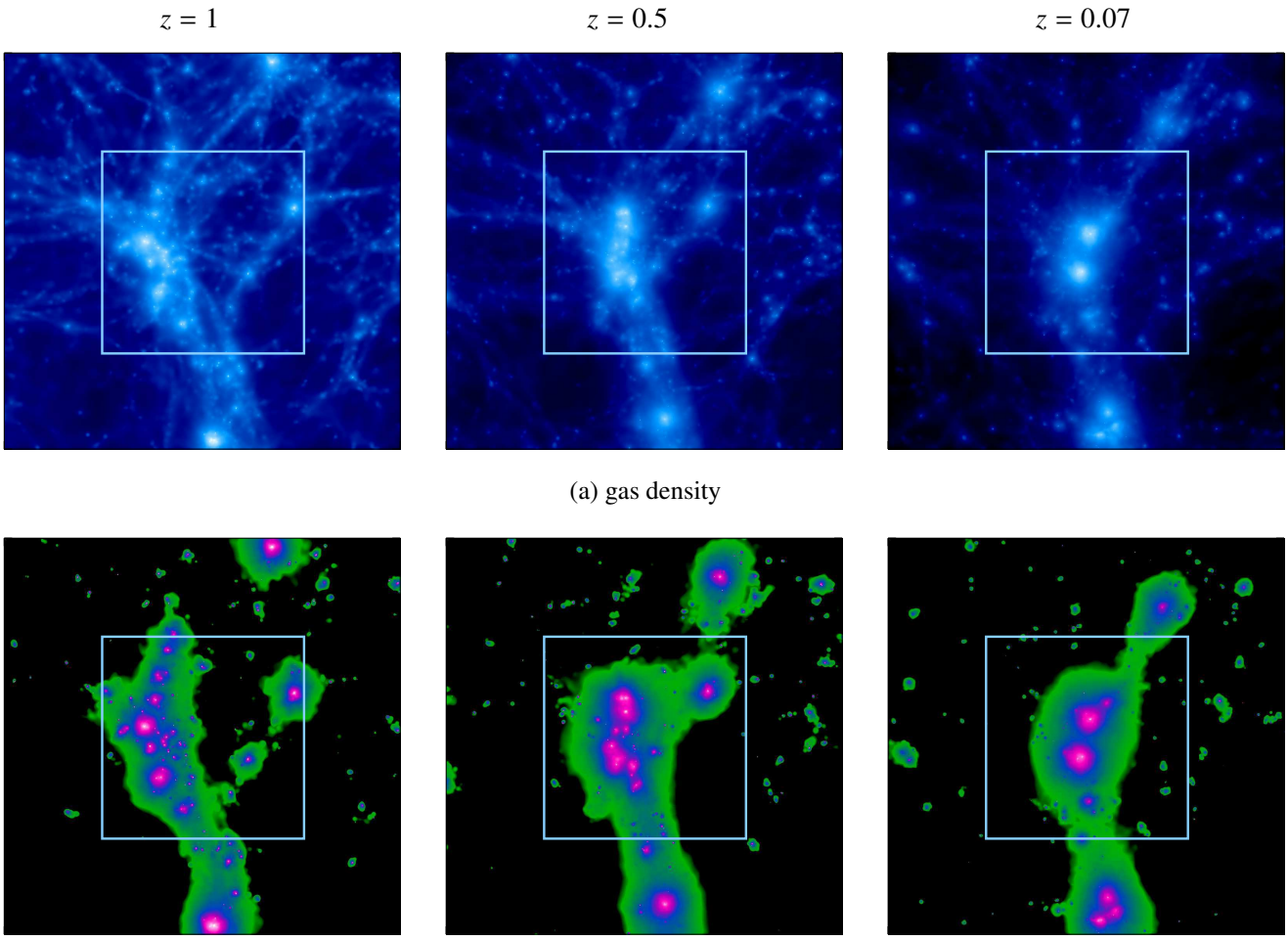

(a) gas density

(b) soft X-ray emission

Fig. 2: Projected maps of gas density and ideal X-ray emission in the [0.5–2] keV band. Each map is $20\,h^{-1}$ cMpc per side, integrated for $20\,h^{-1}$ cMpc along the l.o.s. (z-axis) and centered on the pair center of mass at $z = 0.07$. The squares ($10\,h^{-1}$ cMpc per side) approximate the size of the eROSITA observation.

for asymmetries in the mass distribution of the clusters does not affect our conclusions.

We primarily consider the volume within a radius of $500\,h^{-1}$ ckpc from the spine, namely ~ 660 kpc for the chosen redshift and cosmology, to focus on the core of the bridge and investigate the gas origin and properties. This radius approximately corresponds to $\sim 0.8 \times R_{500}$ for both clusters. We adopt here a similar definition as in Brüggen et al. (2021), who investigate the bridge of thermal gas between A3395 and A3391 that was recently observed with eROSITA, to search for signatures of radio synchrotron emission. Indeed, they also define the bridge as a cylindrical volume with a radius of 600 kpc, and a length of 1.3 Mpc (see Sec. 5 for further discussion).

A schematic view of the system and the bridge, rotated to visualize the maximum physical distance between GC1 and GC2, is reported in Fig. 3. The bridge gas thus defined is also marked in blue in Fig. 1. The gas mass in the bridge thus defined is roughly $\sim 10\%$ of the gas mass comprised within R_{200} of either cluster in the pair.

4. Results

4.1. Origin of the pair system

In Fig. 4 we show the evolution of the system at four redshifts between $z \sim 0.47$ and $z = 0.07$. The gas density maps, projected along the three major axes of the simulations (z, y and x from left to right), comprise the local environment within a comoving volume of $(20\,h^{-1}\,\mathrm{cMpc})^3$ centered on the pair center of mass. In addition to the pair members GC1 and GC2, we also mark the position and R_{200} extent of the most massive groups identified at $z = 0.07$ in the region (see Sec. 4.4, in the following). The maps allow to follow the assembly of the knot region in the last ~ 4 gigayears, and the complicated three-dimensional geometry connecting the multiple haloes and filaments around it.

Filamentary structures in the gas distribution are observed in all maps, with a complex three-dimensional geometry. In fact, several gaseous filaments can be noticed, even without significant group-size haloes located in them, such as those in the regions left and right of the main halo chain in the z-projection (left panels). These are also recognizable in the other two projections. Such minor filaments, however, are expected to be faint in the X rays, as noticed from the lower panels in Fig. 2. From the redshift evolution in Fig. 4 we follow the whole region, fil-

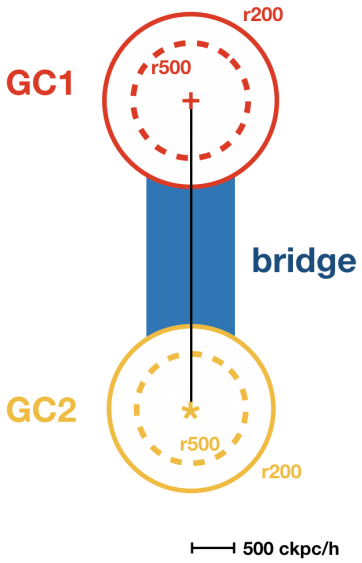

Fig. 3: Schematic view of the simulated system and bridge, rotated to maximize the physical separation between GC1 and GC2.

aments and haloes, collapsing to form the central Cosmic Web knot, where the cluster pair is finally located.

Focusing in particular on the pair system, simulations allow us to explicitly investigate the origin of the gas between the two member clusters. It is evident, from the evolution of the halo progenitors shown in Fig. 4, that the pair members GC1 and GC2 have not merged yet by $z = 0.07$. Despite the R_{200} of GC1 and GC2 almost overlap in the reference projection (see Fig. 1, left), we remind here that the two clusters are indeed physically separated by a larger distance (namely, by two times the sum of their R_{200} radii, as described in Sec. 3.1) — which might also be the case for the observed A3391/95 system (Tittley & Henriksen 2001; Reiprich et al. 2021), although it is difficult to assess the true physical separation from redshift arguments only. In the simulations, we can explicitely visualize this from the additional projections along the y and x axes in Fig. 4 (last row, central and right-hand-side panels).

Here, we aim at assessing whether the gas in the bridge can be stripped gas from the outer atmosphere of the two clusters or rather true filament-like gas. To this end, we select the gas that resides within GC1, GC2 and in the interconnecting bridge at $z = 0.07$, and track it back in time. For the two GC1 and GC2 clusters, we consider all the gas particles enclosed within their R_{500}. The gas bridge is selected in the region between GC1 and GC2, as defined in Sec. 3.1.1

For each selection, Fig. 5 shows the evolution of the gas distances from the closest cluster progenitor, between redshift $z = 0.47$ and $z = 0.07$. In particular, the red dashed and yellow solid lines refer to the gas residing within R_{500} from GC1 and GC2, respectively. The blue dotted line marks the gas selected within the pair bridge.

We find that the bulk (90–95%) of the gas in the bridge at $z = 0.07$ was never inside R_{200} of either cluster progenitor, and a large majority ($\gtrsim 80\%$) was actually always beyond $2 \times R_{200}$ down to $z \sim 0.25$. Since $R_{\rm vir} \sim 1.5 \times R_{200}$, $\gtrsim 80\%$ of the bridge gas was essentially never within the virial radius ($R_{\rm vir}$) of the clusters main progenitors.

At lower redshifts, when the pair system approaches the final configuration, the gas bridge is more and more confined between R_{200} and $2 \times R_{200}$, where it is finally identified. From our analysis, we conclude that the diffuse gas in the bridge in this case is mostly filament-like and comprises only a minor fraction of gas which was mixed in from the outer atmosphere of the two main clusters.

Compared to the bridge gas, Fig. 5 shows that the gas selected within R_{500} in both clusters has been more smoothly accreted during their formation history. Below $z \sim 0.25$ it almost entirely resides already within $2 \times R_{200}$. Both GC1 and GC2 undergo significant mergers, which occur at $z \lesssim 0.5$ for GC1 and more recently, at $z \sim 0.2$, for GC2. The latter, in particular, is clearly shown in the top-right panel of Fig. 5, where the two clear components in the gas distance distribution of GC2 (yellow solid line) approach and merge between $z \sim 0.25$ and $z \sim 0.14$ (also visible from the gas density maps in Fig. 4). In the case of GC2, a significant fraction of the gas selected within R_{500} at $z = 0.07$ comes from the merger, as $\sim 55(34)\%$ of it is still beyond R_{200} at $z \sim 0.25(0.18)$. Differently, most (70%) of the gas finally residing within R_{500} of GC1 is already within its virial boundary ($< R_{200}$) by $z = 0.25$, whereas only $\sim 5\%$ is farther than $2 \times R_{200}$. From this, we therefore also conclude that the gas within the R_{500} of GC1 does not come from the northern group B, which is finally entering the atmosphere ($R_{\rm vir}$) of GC1 at $z \sim 0.16$ for the first time. Compared to the observed A3391/95 system, this is consistent with a picture where the ICM of the Northern Clump, located at $3 \times R_{200}$ relative to A3391, has not yet been stripped and mixed in with the ICM of A3391.

Fig. 6 visually shows the spatial origin of the gas particles of the three aforementioned components through their trajectories towards their final positions at $z = 0.07$. In the background, we report the projected gas density maps in the $(20\,h^{-1}\,{\rm cMpc})^3$ comoving volume centered on the pair (same as Fig. 4-bottom row). The lines mark the trajectories of the gas in the different components, from their position at $z \sim 2$ till $z = 0.07$. The colors distinguish the gas in GC1, GC2 and in the bridge between them (red, yellow and blue respectively; as in Fig. 5), with a color gradient from early times (dark) till $z = 0.07$ (light). In order to ease the visualization, we only show the trajectories for 1000 randomly-selected gas particles, for each gas component. From the visual inspection of the trajectories, we note that the gas in the bridge (blue lines) is actually collapsing from directions almost orthogonal to the main accretion directions of the gas selected from the clusters (red and yellow lines).

4.2. Thermal and chemical properties of the diffuse gas

Given the geometrical configuration presented by this system, with a large physical separation relative to the R_{200} of the member clusters and a mostly independent origin of the majority of gas in the bridge, this is an optimal target to study the thermo-chemical properties of the warm-hot gas populating cosmic filaments in comparison to ICM in clusters. Observationally, hints for the presence of colder gas in the interconnecting bridge of the A3391/95 system have been in fact found by *eROSITA* (Reiprich et al. 2021) as well, encouraging a deeper dedicated spectroscopic analysis of the warm gas in the bridge (Ota et al. 2021, in prep.).

In the simulated system, GC1 and GC2 are small-size clusters with mass-weighted average temperatures of $T^1_{\rm mw,500} = 2.60\,{\rm keV}$ and $T^2_{\rm mw,500} = 2.93\,{\rm keV}$, respectively. As often done in simulation analysis for a better comparison to X-ray obser-

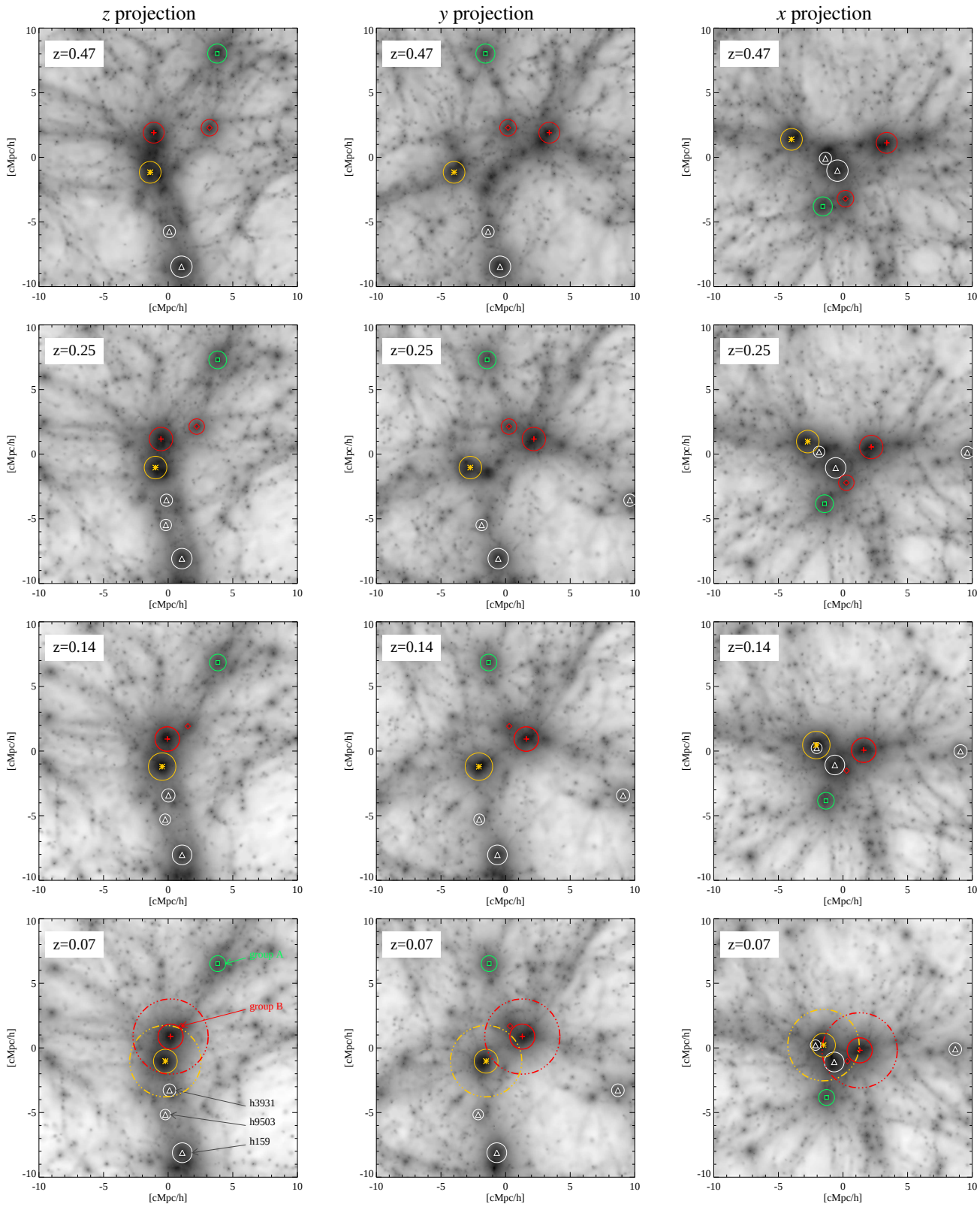

Fig. 4: Evolution of the main haloes in the pair region, in the three main projection axes (z, y and x, from left to right). The maps show projected gas density within a $(20\,h^{-1}\,\mathrm{cMpc})^3$ comoving volume centered on the final (at $z = 0.07$) pair center of mass, for different redshifts between $z = 0.47$ and $z = 0.07$ (from top to bottom). We mark GC1 and GC2 (red cross and yellow asterisk, respectively), the two northern groups A and B (green square and red diamond), and the additional main group-size haloes in the region (white triangles), and their progenitors. For each halo, circles approximate their R_{200} extent, except for group B at $z \lesssim 0.16$, when it is identified as a substructure gravitationally bound to GC1. For GC1 and GC2, the dot-dashed circles at $z = 0.07$ correspond to $3 \times R_{200}$.

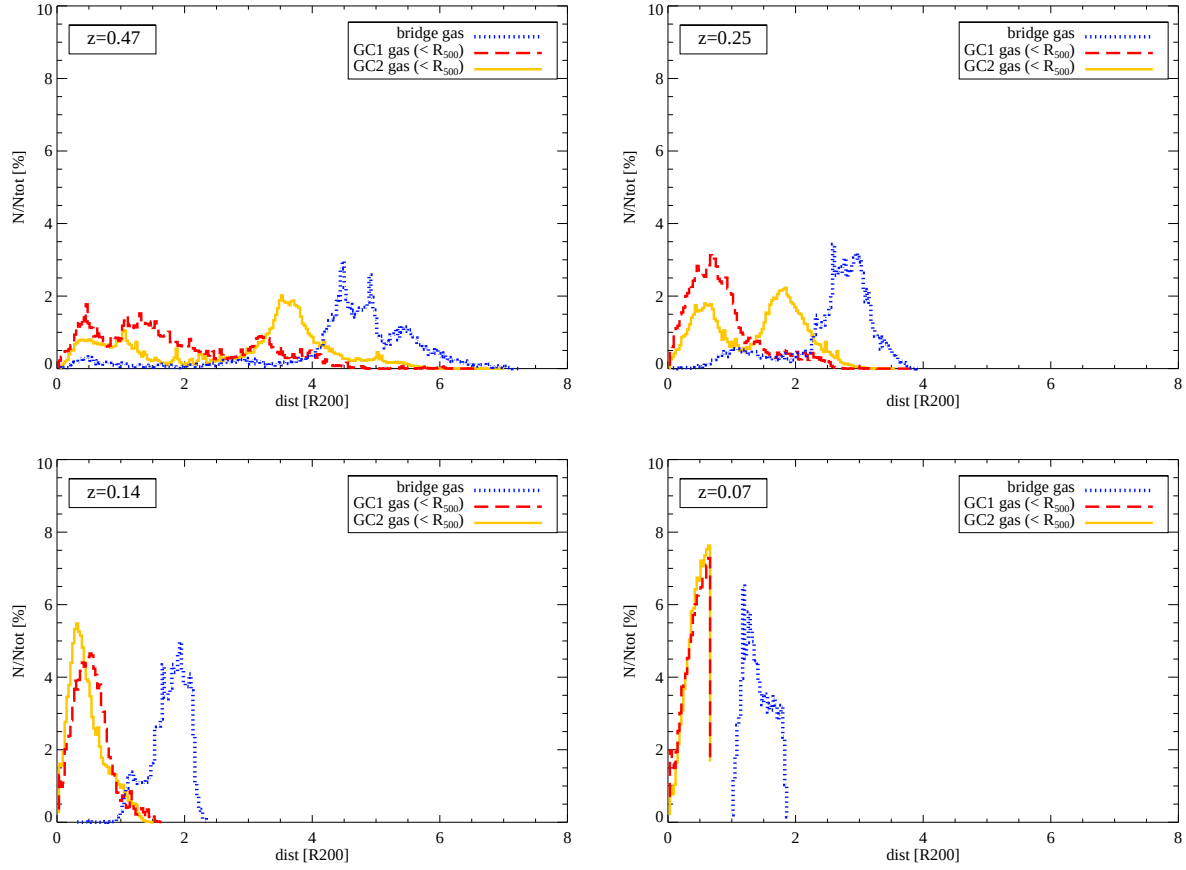

Fig. 5: Evolution between $z \sim 0.47$ and 0.07 of the gas distance with respect to the closest progenitor of the two pair members, in units of its R_{200} at the given redshift. Gas is selected at $z = 0.07$ within the bridge (blue dotted line) or within R_{500} of each cluster (GC1: red dashed line; GC2: yellow solid line).

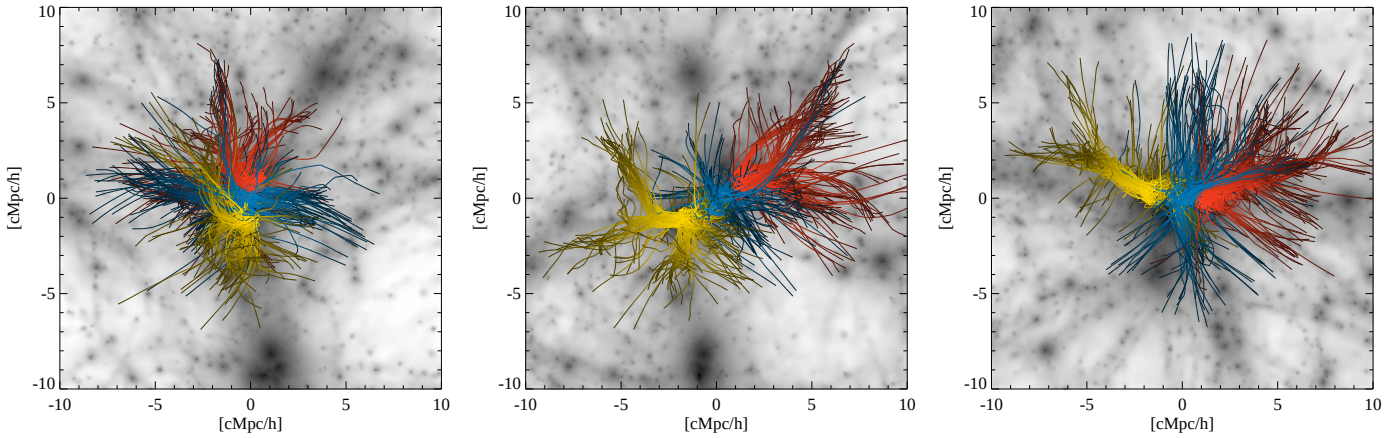

Fig. 6: Gas density maps in the three main projection axes (z, y and x simulation axis, from left to right) at $z = 0.07$. Each map, centered on the cluster pair, encloses a cubic volume of $20\,h^{-1}$ cMpc per side. Overplotted in red, yellow and blue, the spatial trajectories of the gas particles finally selected within R_{500} of GC1 and GC2 and in the bridge at $z = 0.07$. Each trajectory shows a color gradient with time, from dark at $z \sim 2$ to light at $z = 0.07$.

vations, we can estimate a spectroscopic-like ICM temperature ($T_{\rm sl}$), i.e. an average temperature weighted by $\rho^2 T^{-0.75}$ (Mazzotta et al. 2004) instead of gas mass. In this case, we obtain $T^1_{\rm sl,500} = 2.03\,{\rm keV}$ and $T^2_{\rm sl,500} = 2.64\,{\rm keV}$, for GC1 and GC2 respectively.

In Fig. 7, we show a zoom-in mass-weighted temperature map of the system at $z = 0.07$, projected along the z-axis, with the two main clusters GC1 and GC2 and their R_{500} radii marked. The map comprises a region of $7\,h^{-1}$ cMpc per side, centered on the cluster pair center of mass. From the map we note that a radial gradient in temperature is present in both systems with higher temperatures ($\gtrsim 3.5\,{\rm keV}$) in the cores. As for GC2, we also note an asymmetry in the innermost region, with a more extended high-temperature core. This is related to the presence

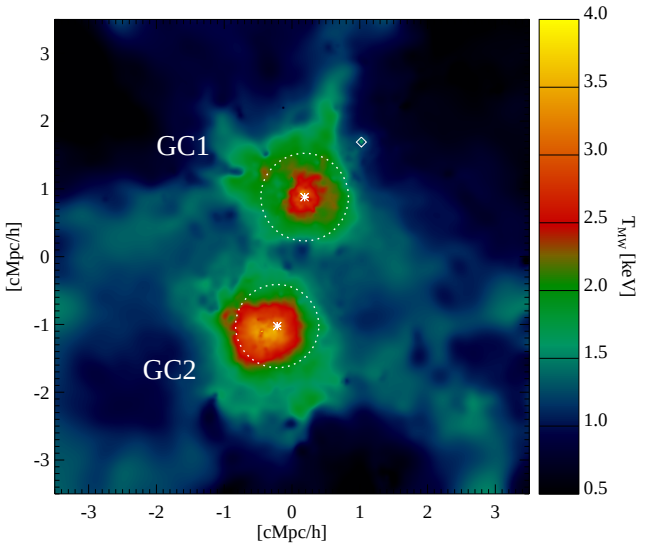

Fig. 7: Projected mass-weighted temperature map of the galaxy cluster pair at $z = 0.07$. The map is centered on the system center of mass and is $7\,h^{-1}$ cMpc per side, and the integration along the l.o.s. is also performed over $7\,h^{-1}$ cMpc. The white dotted circles idicate the R_{500} radii of GC1 and GC2. The position of group B (diamond) is also marked.

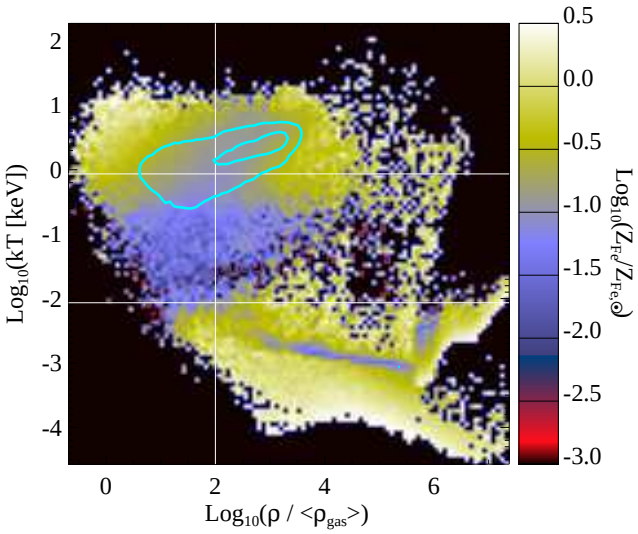

Fig. 8: Density-temperature phase-space diagram of the gas in the $(7\,h^{-1}$ cMpc$)^3$ region centered on the cluster pair at $z = 0.07$, color-coded by gas Fe abundance (in solar unit w.r.t. Anders & Grevesse (1989)). Overplotted, the contours (cyan lines) enclosing $\sim 25\%$ (inner) and $\sim 75\%$ (outer) of the selected gas mass.

of two main substructures, i.e. galaxies, that recently merged (~ 3 Gyr ago; see also Fig. 5 and according discussion). Within R_{500}, we note in fact that GC2 presents an overall hotter ICM with respect to GC1, despite having a smaller mass. In the region between the two clusters, we notice from the color code the presence of colder (bluer) gas, which can be linked to the bridge connecting the two clusters (see also Reiprich et al. 2021). In Fig. 7, one can further see the colder region on the top-right corner, which corresponds to the smaller group-size halo that is approaching R_{200} of the GC1 cluster (diamond; group B). At $z = 0.07$, this sub-halo is found to be already gravitationally bound to GC1, with the merging starting at $z \sim 0.16$

In Fig. 8 we report the density-temperature phase-space diagram of the gas particles enclosed in the $(7\,h^{-1}\,\mathrm{cMpc})^3$ region already shown in Fig. 7. The gas density is here reported in terms of overdensity w.r.t. the mean background baryon density of the simulation, $\delta \equiv \rho / <\rho_{\rm gas}>$. The vertical line in the diagram corresponds to an overdensity of $\delta = 100$, whereas the horizontal lines mark the temperature thresholds $T = 10^5$ K and $T = 10^7$ K. In this way, we can easily separate interesting gas phases depending on its temperature and density (see also Cen & Ostriker 2006; Ursino et al. 2010; Martizzi et al. 2019). We define "hot" gas the phase with $T > 10^7$ K (roughly corresponding to $T > 1$ keV). This is typically the gas within deep potential wells, such as those of galaxy clusters or groups, as well as in shocks. The warm gas, instead, is defined as the gas with $10^5 < T[\mathrm{K}] < 10^7$. In terms of density, the diffuse gas that is expected to fill the filaments and bridges interconnecting clusters in the large-scale structure is typically characterised by overdensity of ~ 100 or lower. In particular, we refer here to the so-called warm-hot intergalactic medium (WHIM) as the gas with $10^5 < T[\mathrm{K}] < 10^7$ and $\delta < 100$.

The color-code in Fig. 8 marks instead the gas Fe abundance, weighted by the gas mass in each temperature-density bin. From the inspection of the phase diagram, we note that the hot phase and the dense and cold gas are typically characterised by the highest abundance level, with Fe abundances around the solar value or higher. The low-density gas is characterised by a lower Fe abundance, $Z_{\mathrm{Fe},\odot} \sim 0.01$–$0.1$ (see also following Sections), especially when the warm phase ($10^5 < T[\mathrm{K}] < 10^7$) is considered.

We overplot contour lines (cyan curves) to mark the regions where $\sim 25\%$ and $\sim 75\%$ (inner and outer curves, respectively) of the total selected gas mass is located. From these, we notice that the majority of the gas mass ($\sim 75\%$) in the pair and its surroundings is in the warm and hot phase, and with overdensities between a few and ~ 2500. The gas in smaller haloes (low temperatures and high densities), and the hot low-density gas associated to feedback processes, only contribute $\sim 10\%$ of the gas mass in the whole region.

For comparison, in Fig. 9 we show instead the density-temperature diagram for the gas included in one of the two pair members (upper panel), and in the bridge (lower panel). As an example, we select the GC1 cluster and show the gas enclosed within its R_{200} radius, in Fig. 9a. The phase-space diagram is therefore only populated at overdensities larger than ~ 100. As indicated by the external contour level, 75–80% of the GC1 gas mass within R_{200} has $T \gtrsim 10^7$ K and median overdensities $\delta \sim 1000$, as marked by the mass-weighted values reported in the diagram (dot-dashed lines). From the temperature-density distribution we also note that the gas hot phase ($T \gtrsim 10^7$ K) shows a gradient in the Fe abundance: at lower densities the typical metallicity is also lower. This essentially corresponds to the X-ray emitting ICM, for which the radial abundance profile is indeed expected to be a decreasing function of the cluster-centric distance (see Mernier et al. 2018; Biffi et al. 2018b, for recent observational and numerical reviews), with larger values in the central regions (corresponding to higher overdensities) and lower values in the outskirts (at lower overdensities). The cluster potential well also comprises high-density cold gas, which is typically found in (or close to) star-forming regions, or within substructures, e.g. galaxies. Typically, this is consequently char-

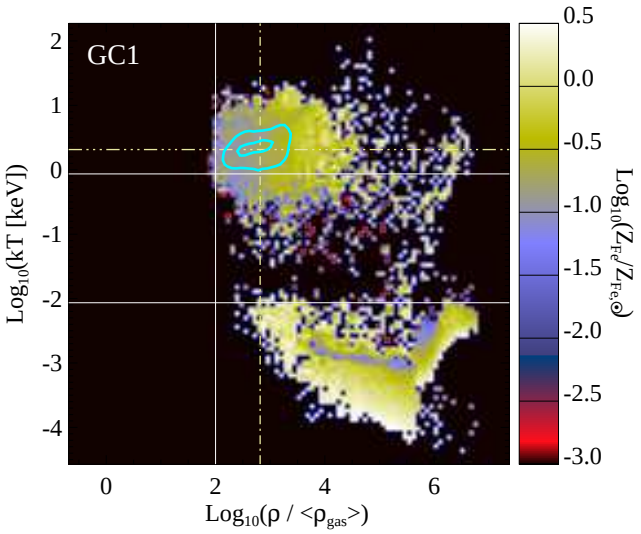

(a) GC1.

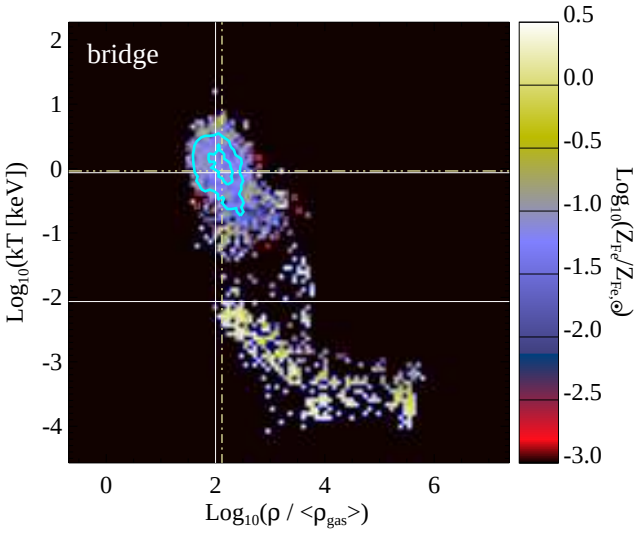

(b) Bridge.

Fig. 9: Same as Fig. 8, but only for the gas within R_{200} for one of the member clusters, namely GC1 (upper panel) and for the gas in the bridge (lower panel) between the pair clusters, at $z = 0.07$. Dot-dashed lines mark the average temperature and overdensity values (mass-weighted estimate) of the selected gas.

acterised by large values of the metallicity, as it has been more easily polluted by stellar sources. Although we only show the case of GC1, as an example for the pair clusters, we verified that the density-temperature diagram of GC2 presents very similar features.

Fig. 9b shows that the majority of the gas in the core of the pair bridge (i.e. closer than $< 500\,h^{-1}$ ckpc from its spine and outside the R_{200} of either cluster; Sec. 3.1.1) occupies the upper envelope of the distribution, as marked by the mass contours. Specifically, we find that in the simulated system $\sim 75\%$ of the gas mass in the bridge is in the warm-hot phase, with a typical temperature of ~ 1 keV, a median overdensity of ~ 100 (marked by the dot-dashed lines) and an homogeneous iron abundance of $Z_{\rm Fe} \sim 0.1\,Z_{\rm Fe,\odot}$. The colder phase of the WHIM, with $T \sim 10^5$–10^6 K and $\delta \lesssim 100$, is not significant. This is consistent with recent simulation results, e.g. by Galárraga-Espinosa et al. (2020b), who find the presence of hot gas within 1 Mpc from the spine of short filaments. At larger distances from the filament spine they predict the colder WHIM phases to dominate. By enlarging the bridge radius up to $1\,h^{-1}$ cMpc (approximately 1.3 Mpc in physical units), we also confirm a shift of the gas mean overdensity towards lower values $\delta \lesssim 100$. Finally, from Fig. 9b, we find that a minor fraction of the bridge gas mass is characterised by large values of overdensity and iron abundance, and low temperatures ($T \lesssim 10^5$ K). This is halo gas associated to galaxies, either comprised within small substructures or stripped from galaxies at earlier times. The presence of a small, albeit non negligible, fraction of halo gas in short filaments is similarly reported by Galárraga-Espinosa et al. (2020b).

Overall, in such a system, the bridge gas closely reflects the chemo-energetic properties of the WHIM, with average temperature and density clearly lower than the ICM within the two clusters. Combined with the analysis of its spatial origin (Sec. 4.1), this further supports the conclusion that this is filament-like gas and not stripped ICM due to the interaction between the pair clusters.

Metallicity distribution. Fig. 10 shows the iron abundance distribution for the gas in the $(7\,h^{-1}\,{\rm cMpc})^3$ volume around the pair at $z = 0.07$, for different thermal phases and spatial selections. In particular we consider six cases: all the gas in the hot phase ($T > 10^7$ K; black), the warm gas ($10^5 < T[{\rm K}] < 10^7$; solid grey), the WHIM ($10^5 < T[{\rm K}] < 10^7$ and $\delta < 100$; dot-dashed grey), the X-ray-emitting ICM in GC1 and GC2 (with $T > 0.3$ keV, and located inside R_{200}; red and yellow respectively) and the gas selected in the bridge between them (blue; defined as in Sec. 4.1). In the Figure we report the number distribution of iron abundance (upper panel) and oxygen-over-iron abundance ratio (lower panel), normalized to the total number of Fe- or O/Fe-rich particles in each gas subsample.

Considering the iron abundance (Fig. 10, top), we note that a broad double-peak feature is common to all curves, with differences in the gradient of the low-abundance tail and the relative amplitude of the peaks depending on the gas selection considered. The two peaks roughly correspond to abundances of $Z_{\rm Fe} \sim 10^{-3}$–$10^{-2}\,Z_{\rm Fe,\odot}$ and to solar values ($\sim Z_{\rm Fe,\odot}$), respectively. For the bridge gas, the low-metallicity peak is further shifted to $\sim 10^{-4}\,Z_{\rm Fe,\odot}$, with a more extended valley between the two peaks. Despite the differences, we note that the mass-weighted abundance of each sample is always of order $\sim 10^{-1}\,Z_{\rm Fe,\odot}$, namely between $0.1\,Z_{\rm Fe,\odot}$ for the warmer phases and $0.2\,Z_{\rm Fe,\odot}$ for the ICM/hot gas[4]. Compared to other selections, the whole hot-phase gas and the ICM residing within clusters typically show a similarly steeper low-metallicity tail and a more pronounced peak at low metallicity relative to the solar-metallicity one. Overall, a large fraction of the ICM is significantly enriched, with abundances $\gtrsim 10^{-2}\,Z_{\rm Fe,\odot}$. Compared to the hotter gas phases, for the gas in the warm phase and the WHIM, the low-metallicity tail is shallower and has a higher normalization (consistently with previous studies, e.g. Cen & Ostriker 2006), with a shallower peak at abundances $\sim 10^{-3}\,Z_{\rm Fe,\odot}$. This broad low-abundance component extends down to even lower values, $\sim 10^{-4}\,Z_{\rm Fe,\odot}$, for the gas in the core of the pair bridge. Essentially, we can divide the different gas selections into two broad categories based on the trends shown in Fig. 10: the hotter

[4] We note that, for the ICM in GC1 and GC2, the global estimate within R_{200} is dominated by the outer lower-density regions, where the bulk of the cluster mass resides — see also mass contours in Fig. 9a.

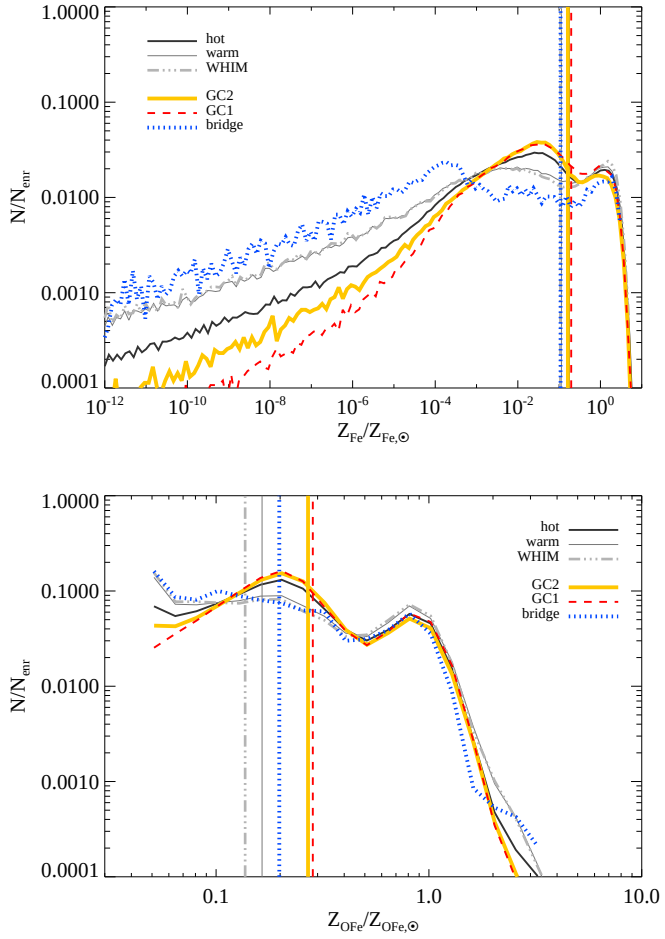

Fig. 10: Distributions of Fe abundance and O/Fe abundance ratio for the gas selected at $z = 0.07$ in different spatial regions and thermal phases. For each gas selection, the corresponding distribution is normalized to the total number of enriched (i.e. $Z_{\rm Fe} > 0$ or $Z_{\rm OFe} > 0$) gas particles.

gas within the main clusters and the warmer, lower-density gas phase.

The warm diffuse gas outside the main clusters and in the bridge is typically poorly enriched. It always comprises, nevertheless, a highly-enriched component originating from, or still associated to, galaxy-size haloes. This is responsible for the distribution peak centered on solar abundances.

A broad similar distribution is found for the oxygen abundance, with the main difference that both peaks are more pronounced and the peak at lower abundances is broader and shifted towards lower values. This can be investigated via the O/Fe abundance ratio, shown in the lower panel of Fig. 10. The oxygen-to-iron ratio distribution shows in all cases a very similar peak around solar values, originated by the corresponding solar-abundance peaks present in both iron and oxygen distributions. Small differences are still observed between hot/cluster gas and warmer/bridge plasma in the left-hand-side tail of the distribution. This is in fact broadly flat for the warmer gas phases, whereas presents a secondary peak for the hot ICM and a decrease towards $Z_{\rm OFe} \lesssim 0.1\, Z_{\rm OFe,\odot}$. The mass-weighted average O/Fe ratio is three times lower in the warm phase than within clusters, indicating that a larger fraction of warmer gas has very small O/Fe abundance ratio. This is consistent with the fact that the vast majority of warm diffuse gas is expected to be located far from dense star-forming sites which are primarily responsible for oxygen enrichment.

4.3. Evolution of gas chemical properties

Given the possibility to track back in time the gas particles selected at $z = 0.07$, we investigate the evolution of the gas chemical properties depending on its *final* location or thermal phase. This is shown in Fig. 11 for the gas selected at $z = 0.07$ within GC1 (top) and in the pair bridge (bottom), representative of the hotter and warmer phases respectively. In the four panels of the figure we report the redshift evolution between $z = 4.3$ (purple curves) and $z = 0.07$ (red curves) of the iron abundance (l.h.s. panels) and O/Fe ratio distributions (r.h.s. panels) of these two gas subsamples.

From the evolution of the iron distribution we can infer two general trends: the gas that is finally selected in the hot phase and in clusters has undergone a stronger evolution in time compared to the gas that is finally located in the warm, low-density gas, like the WHIM or the gas selected within the pair bridge. In fact, comparing the two l.h.s. panels in Fig. 11, we note that the shape of the iron abundance distribution changes in time in the GC1 case, whereas the gas finally selected in the bridge shows little variation, especially in the low-metallicity tail. The mass-weighted abundance, nevertheless, increases with time in both gas subsamples, indicating that the mass fraction of highly enriched gas increases in both cases at low redshift. The solar-abundance component noted in Fig. 10 seems to be present already from $z \lesssim 2$–3 (blue and cyan lines). This can be observed also from the evolution of the O/Fe abundance ratio distribution, in the r.h.s. panels of Fig. 11, where a peak around solar values is always present below $z \lesssim 3$ and is more prominent at high redshift, where it is driven by SNII oxygen enrichment. The latter is also responsible for the higher values of the O/Fe abundance ratio reached at high redshifts, where the right-hand-side tail is higher in normalization and more extended. This confirms that part of the gas has been enriched already at early times (especially with oxygen) and survives in the diffuse form till $z = 0.07$ (see also Biffi et al. 2018a). Residual, late-time enrichment is driving the change in the O/Fe distribution at lower values, where a central peak around $Z_{\rm OFe} \sim 0.2\, Z_{\rm OFe,\odot}$ is building up at low redshift, more prominently in the hot ICM within GC1 than in the gas ending up in the bridge. The gas selected within the bridge, differently, shows a shallower distribution at central O/Fe values, although some increase is also visible and the peak at solar values still decreases in time relative to the lowest abundance ratios. This can still be attributed to late iron pollution due to long-lived SNIa.

While Fig. 11 shows the differences in the distribution shape at different redshifts, we also verified that, despite preserving the general shape features, the normalization of the curves increases with time when the distributions are computed in terms of gas mass (see Appendix C), and normalized at each redshift to the total mass of the selected gas. Indeed, the mass fraction of iron- and oxygen-rich gas increases with time. This picture is summarized by the trends shown in Fig. 12, where we quantify the redshift evolution of the star-forming (i.e. with instantaneous SFR > 0) and enriched ($Z_{\rm Fe} > 0$) gas fractions with respect to the total gas mass, for each gas selection. There we can notice how the enriched gas fraction increases with redshift in all cases analysed, with $\sim 90(50)\%$ of the hot(warm) gas finally enriched by $z = 0.07$. Over the whole redshift range, $0.07 \lesssim z \lesssim 4$, the gas in the hot phase and within clusters at $z = 0.07$ was sys-

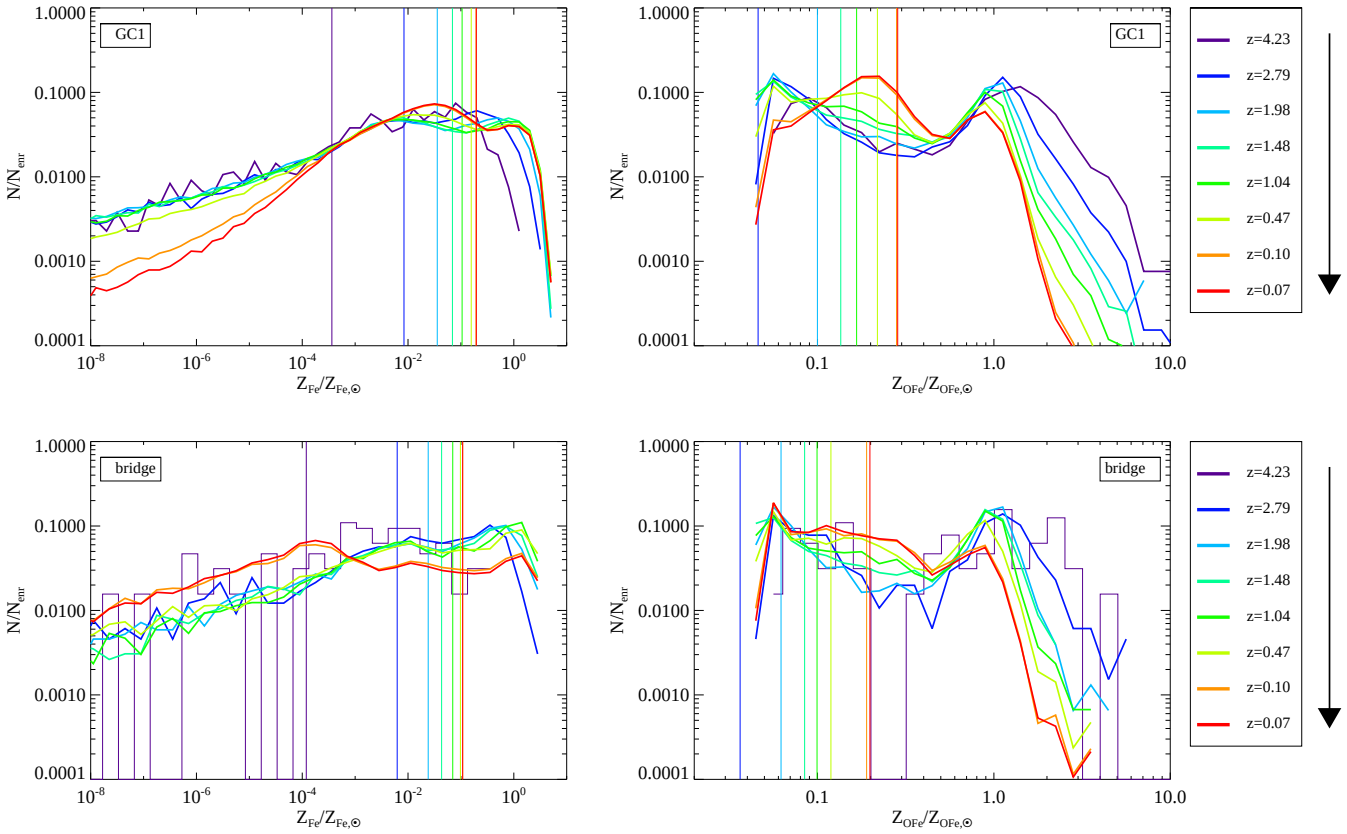

Fig. 11: Redshift evolution of the iron abundance (left) and O/Fe abundance ratio (right) distributions for the ICM in one of the clusters (GC1; top) and the bridge gas (bottom), selected at $z = 0.07$ and tracked back in time. Vertical lines mark the MW-average abundance at any corresponding redshift. The bridge histogram line for $z = 4.23$ is thinner to mark the very low statistics of metal-enriched gas particles (only $\lesssim 100$, i.e. $\sim 0.6\%$ of the total).

tematically more enriched by a factor of ~ 1.7, compared to the gas that is finally in the warmer phases. The gas that will end up in the bridge shares a chemical evolution similar to the diffuse, warmer phases down to $z \sim 0.5$. At lower redshifts, however, the mass fraction of the (poorly) enriched component increases more significantly in the bridge gas then in the warm/WHIM case.

In Fig. 12 we also show the time evolution of the highly-enriched gas mass fraction, which we define as the mass fraction of the selected gas particles that at any given redshift have an iron abundance larger than the mass-weighted average value computed at $z = 0.07$ (i.e. with $Z_{\rm Fe} > Z^{z=0.07}_{\rm Fe,mw}$). Similarly, this also grows in time. Such highly-enriched component, nevertheless, was already present at high redshift in all selections, and typically increases by a factor of ~ 3 in mass between $z \sim 2$ and $z = 0.07$. Only for the ICM selected at $z = 0.07$ within the two clusters it increases more prominently (by a factor of $\gtrsim 4$). Although not shown here, an overall similar, albeit shallower, trend is observed for oxygen, with less pronounced differences among the various gas selections. The curves shown in the bottom inset of Fig. 12 show that the gas selected in the different cases at $z = 0.07$ has always undergone a peak of star-formation activity around $z \sim 2$. Wherever the gas is finally residing, at the peak of star formation the mass fraction of tracked gas that was star forming is of order of a few percent at most. Differently, at redshifts $z \gtrsim 3$ the star forming gas adds up to less than 1% of the total mass of the gas selected, with slightly higher values for the gas that is ending up within structures and negligible or zero

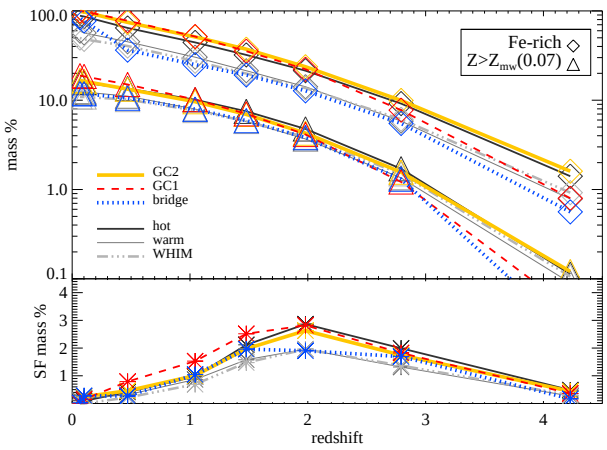

Fig. 12: Evolution with redshift of enriched and star-forming mass fractions for the gas in different spatial regions and thermal phases, selected at $z = 0.07$ and tracked back in time. *Upper inset:* mass fraction of Fe-rich gas ($Z_{\rm Fe} > 0$; diamonds) and highly-enriched gas ($Z_{\rm Fe} > Z^{z=0.07}_{\rm Fe,mw}$; triangles). *Lower inset:* redshift evolution of the star-forming (SFR > 0) gas mass fraction.

star formation in the other cases. This trend is also observed at $z \lesssim 1$, with no star-forming gas within clusters at $z = 0.07$, by definition.

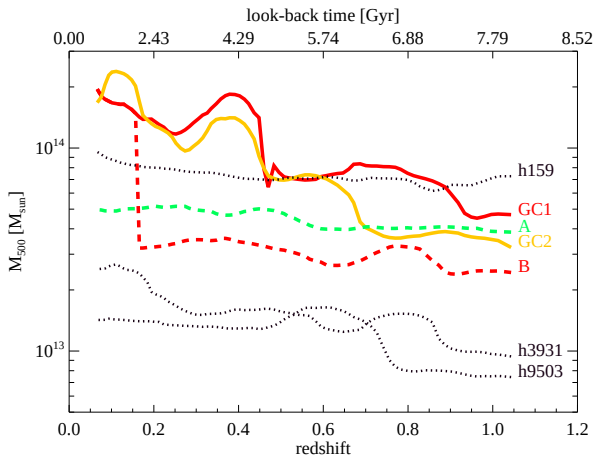

Fig. 13: Redshift evolution of the total mass M_{500}, for all the clusters and groups identified at $z = 0.07$ in the $(20\,h^{-1}\,\mathrm{cMpc})^3$ volume around the cluster pair. At each redshift up to $z \sim 1$, we consider the main progenitor of the given halo identified at $z = 0.07$.

4.4. Additional structures in the local environment

Several other extended sources, the size of groups and clusters of galaxies, have been detected in the *eROSITA* PV observation of the A3391/95 field, a number of which at the same redshift of the pair system (Reiprich et al. 2021, Ramos-Ceja et al., in prep.). Similarly, in the local environment surrounding the simulated cluster pair we find additional massive structures, all comprised within the considered volume of $20\,h^{-1}$ cMpc per side (about 26 Mpc for the redshift and cosmology considered). In the simulations, we identify in particular 4 group-size haloes with masses in the range $M_{500} \sim 1.4$–$9.6 \times 10^{13}\,\mathrm{M}_\odot$. Additionally, we consider the aforementioned group B, a structure with the size of a small galaxy group, that has entered the atmosphere of GC1 at about $z = 0.16$ and has reached its outskirts by $z = 0.07$ (when is located at $d_{3\mathrm{D}} \sim 1.5 \times R^{1}_{200}$). At $z \lesssim 0.16$ the halo is no more identified as an independent group but rather as a gravitationally-bound substructure of the GC1 cluster, by the SUBFIND substructure-finding algorithm. The position and R_{200} extent of these five systems is also reported in the projected maps of Fig. 4, at different redshifts $z \lesssim 0.5$. For the reference projection at $z = 0.07$ (bottom-left panel in Fig. 4), the haloes are all labelled.

In Fig. 13, we report instead the redshift evolution of the total mass enclosed by R_{500} (M_{500}), for the five groups and the main clusters GC1 and GC2 as well. All the halos, identified at $z = 0.07$, are tracked back in time and the main progenitor[5] is considered at every redshift up to $z \sim 1$. From the Figure, we notice increases in the M_{500} masses of GC1 and GC2, following merging events around redshift $z \sim 0.5$–0.4 and $z \sim 0.2$ (as noticed from Fig. 5).

Motivated by the *eROSITA* observation of the A3391/95 system, where some clumps that appear to be infalling towards the system have been discovered in the Northern and Southern Filament (Reiprich et al. 2021), we concentrate in particular on two systems among those neighbour structures, to search for signatures of motion towards the pair.

[5] For each halo, we always select the most-massive progenitor.

Considering the most massive groups ("h159", "group A" and "group B"; Fig. 13), we focus on the northern-most group A and the smaller group B, respectively marked with the green square and red diamond in Fig. 4. Despite being massive ($M_{500} \sim 6.7 \times 10^{13}\,\mathrm{M}_\odot$), we instead exclude the more complex group h159, which constitutes together with halo "h9503" another close pair, separated by $d_{3\mathrm{D}} \sim 3.5\,h^{-1}$ cMpc and with a mass ratio of almost 7:1. From a deeper inspection, we also notice that the group h159 is a multiple system itself, comprising three massive gravitationally-bound substructures of comparable size ($M_{\mathrm{tot}} \sim 1.4$–$4.9 \times 10^{13}\,\mathrm{M}_\odot$), all within its boundaries ($\lesssim 1.5 \times R_{200}$). Differently, both groups A and B are isolated single structures and yet represent two extreme phases during the infall towards the GC1–GC2 system, with group A still far away from the pair location and group B already merging with one of the member clusters. By inspecting the evolution of group B main progenitor, we find that its mass as a galaxy group is of order $M_{500} \sim 3 \times 10^{13}\,\mathrm{M}_\odot$ (more specifically, varying between $M_{500} \sim 2.5 \times 10^{13}\,\mathrm{M}_\odot$ and $M_{500} \sim 3.6 \times 10^{13}\,\mathrm{M}_\odot$) at redshift $1 \gtrsim z \gtrsim 0.16$, i.e. before entering the GC1 atmosphere (see Fig. 13). Group A is an isolated, more massive group with $M_{500} \sim 5 \times 10^{13}\,\mathrm{M}_\odot$, and is located at a distance of $7.7\,h^{-1}$ cMpc (namely $\sim$ 10 physical megaparsecs) from the pair center of mass, at $z = 0.07$. From Fig. 13 we note that both groups A and B have a rather smooth assembly history, without indications of significant merger events.

In the *eROSITA* A3391/95 field, the Northern Clump (MCXC J0621.7-5242) cluster located in the Northern Filament shows in particular several evidences suggesting a motion towards the A3391 cluster and a possible interaction with the filament gas in which it is embedded. These comprise, for instance, an emission enhancement towards the south, a tail of emission extending towards the north, and a pair of bent asymmetric radio lobes of its central Wide-Angle-Tails (WAT) radio galaxy as well (Brüggen et al. 2021, Veronica et al. 2021). Here, we therefore investigate and compare the signatures of the movement of groups A and B towards the galaxy cluster pair, at redshift $z \lesssim 1$. This is quantified in Fig. 14 (upper insets) by the cosine of the angle ($\cos\theta$) between the group velocity and the direction pointing towards the final position the pair at $z = 0.07$, where the Cosmic Web knot at the center of the whole $(20\,h^{-1}\,\mathrm{cMpc})^3$ region is forming. In the Figure we report the evolution of $\cos\theta$ with redshift, from $z \sim 1$ till $z = 0.07$. For comparison, we investigate the three directions defined by the positions at $z = 0.07$ of the pair center of mass (in blue), GC1 (in red) and GC2 (in yellow) separately. We note from the Figure that the cosine values, for both gas and bulk velocity, are typically comprised between -0.7 and -0.95 below $z \lesssim 1$. This indicates that the velocity component along the infall direction is indeed dominant, and both groups are actually moving towards the cluster pair.

Small differences are nevertheless found in the two cases, with the smaller group B moving more specifically towards GC1 ($\cos\theta$ is significantly lower for the red curve) and eventually merging with it. The value of $\cos\theta$ for the direction towards the final position of GC2 (yellow curves) starts in fact to significantly increase at $z \lesssim 0.5$, marking the divergence of the group B trajectory. Instead, given the larger distance from the knot region, for Group A we find no significant differences for the three directions, especially for redshift $z < 0.5$.

If we consider all the gas within R_{500} (dotted lines), instead of the total bound gas only (dashed lines), then a more significant difference with respect to the halo bulk (DM-dominated; solid lines) velocity is noticed. In fact, the average gas velocity within R_{500} can be influenced by smooth accretion as well as by the in-

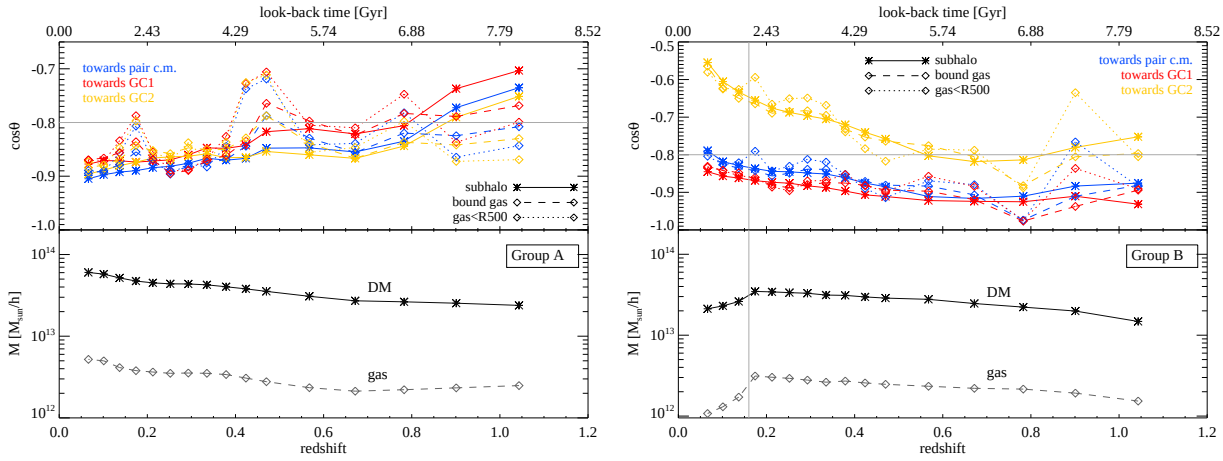

Fig. 14: *Upper panels:* redshift evolution of the alignment between radial direction towards the pair (center of mass, blue; GC1, red; GC2; yellow) and subhalo velocity (as in the legend), quantified by the cosine of the angle between them. For Group B (right), the gas $< R_{500}$ at $z = 0.16$ is tracked to lower redshifts, after entering the GC1 virial boundary. *Lower panels:* redshift evolution of the subhalo DM (solid lines) and gas (dashed lines) bound mass. The two panels refer to groups A (left) and B (right).

fall of substructures onto the group. For group A, these accretion events are visible for instance around redshifts $z \sim 0.75$, 0.45, and 0.2, where the increase in $|\cos\theta|$ is accompanied by a subsequent increase of the subhalo mass (Fig. 14, lower inset). In the case of group B, the accretion of the group itself onto the GC1 cluster is characterised by a corresponding decrease in the group total gas(DM) bound mass by a factor of $\sim 3(1.6)$ between redshifts $z \sim 0.16$ and $z = 0.07$. The decrease of bound mass is the consequence of a stripping phenomenon that group B undergoes while penetrating the atmosphere of the more massive GC1 cluster.

The radial component of the velocity, along the infall direction, is explicitly reported in Fig. 15, across the redshift range $0.07 < z < 1$. We show however the evolution as a function of radial distance instead of redshift, with larger radial distances corresponding to earlier times. As in Fig. 14, we investigate separately the three infall directions and we focus in particular on the velocity of the bound components only, with the bulk velocity essentially dominated by the dark matter. Comparing the two panels in the Fig. 15, we note different trends for the two halos. Group A shows an oscillating behaviour of both gas and bulk velocities, with the oscillations amplified especially in the gas component. This translates into a relative difference between gas and bulk radial velocities swinging between -10% and $+10\%$ throughout the redshift/distance range inspected. Since the feature is preserved in all the three directions considered (always defined with respect to the final positions of GC1, GC2 and pair center of mass), it is indeed associated to the group itself. This is reflecting a sloshing trend of the gas component in the *xy* plane, where the movement along the filament mostly happens, likely due to accretion processes of smaller substructures and diffuse gas from the filaments. This is further confirmed by the center-shift between gas center-of-mass and halo center[6], whose *x* and *y* components visibly present opposite oscillating trends (see Fig. B.1, in Appendix B). While some similar signatures for sloshing are also shown at early times, the smaller group B presents a monotonic increase of the relative difference between the gas and bulk radial velocities, while getting closer than $\sim 2.6\,h^{-1}$ cMpc from GC1, namely below $z \lesssim 0.25$. Even though the reference positions of the pair and its members considered in Fig. 15 are the final ones at $z = 0.07$, we can compute the actual distance between the center of group B and the GC1 progenitor at $z \sim 0.25$, which corresponds to $d_{3D} \sim 3.5\,h^{-1}$ cMpc $\sim 4\times R^1_{200}$. On the *xy* plane, the group B is found at a projected distance of $\sim 3 \times R^1_{200}$ at $z \sim 0.25$. Even though group B does not seem to be located within a main filament, this is the typical distance from clusters at which simulations predict to observe changes in the gas properties along filaments connected to them, such as an increase in the gas temperature and a steeper radial gas density profile (namely at three to four times the cluster virial radius; e.g. Dolag et al. 2006). The configuration of group B roughly ~ 3 Gyr ago and the whole picture shown since then, i.e. between $z \sim 0.25$ and $z \sim 0.16$, is consistent with the properties of the observed Northern Clump in the *eROSITA* A3391/95 field (Veronica et al., submitted), which is in fact located at a similar projected distance of about three virial radii from the A3391 cluster (Reiprich et al. (2021); Veronica et al., submitted).

[6] The center of the halo is defined throughout the paper as the position of the minimum of the halo potential well.

5. Discussion

In this study we investigate properties of a close pair of galaxy clusters showing several similarities compared to the observed A3391/95 system. Given that the simulated analog has been extracted from a cosmological hydrodynamical, not *ad hoc*, simulation, some difference with respect to the observations is naturally present.

In our investigation, we identify the A3391/95 analog by searching among cluster close pairs. We note, however, that the A3395 cluster in the observed system is rather a double merging cluster itself (A3395n/A3395s; Reiprich & Böhringer 2002; Reiprich et al. 2021), even though in the literature it is sometimes treated as a whole, albeit double-peaked, system (Alvarez et al. 2018). The selected simulated pair is instead composed of two clusters, although the GC2 member also comprises two main substructures. These are two massive group-size haloes that underwent a major merging around 3–3.5 Gyr ago ($z \sim 0.3$–0.25, see Sec. 4.1) with a mass ratio of 1:1.6. At the time of merging, the two systems had masses of $M^1_{500} = 7 \times 10^{13}\mathrm{M}_\odot$ and $M^2_{500} = 1.1 \times 10^{14}\mathrm{M}_\odot$, respectively. In fact, two emission peaks

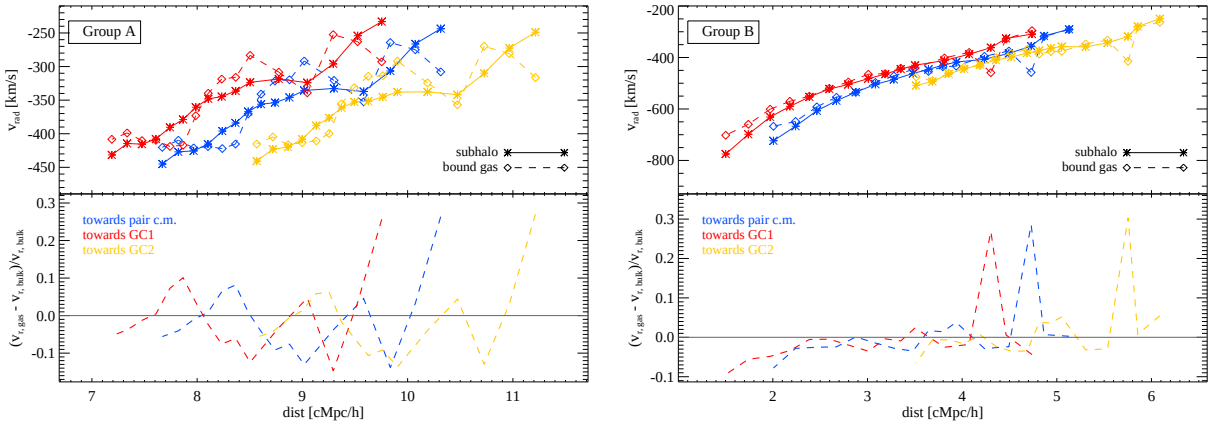

Fig. 15: Radial bulk (solid lines) and bound-gas (dashed lines) velocities (upper panels), and their relative absolute difference (lower panels), for groups A and B (left and right, respectively), as a function of the radial distance from the system (center of mass, blue; GC1, red; GC2; yellow).

are still visible in the innermost regions of GC2 at $z = 0.07$, e.g. in the bottom-right panel of Fig. 2. Compared to A3395s and A3395n, the two structures in the simulated GC2 cluster are at a later stage of interaction. Furthermore, despite this broad similarity, we remind that the overall mass of the system is at least 20% smaller than that of A3391/95, consistent with finding smaller components in GC2 compared to A3395s and A3395n.

Given the smaller masses of the simulated clusters, we can also expect a smaller number of prominent filaments connected to them, as seen in Fig. 2. In fact, numerical studies predict that most of the close pairs of clusters with separation of $5\,h^{-1}$ cMpc or less are typically connected by straight filaments, with less massive clusters connected typically to less filaments (1 or 2, instead of up to 4–5) (Colberg et al. 2005).

In general, some of the structures in the observed A3391/95 system have no direct match in the simulations. This is the case, for instance, of the ESO 161-IG 006 galaxy group located in the bridge region. In the *eROSITA* observations, part of the X-ray emission in the bridge between A3391 and A3395 is associated to the ESO 161-IG 006 group, although not dominated by it. Reiprich et al. (2021) show in fact that the X-ray diffuse emission in the bridge qualitatively spans a horizontal scale of $\sim$ 3 Mpc, larger than the region occupied by the ESO 161-IG 006 group. The definition of the bridge is however somewhat uncertain. Brüggen et al. (2021) model the bridge in A3391/95 as a cylindrical volume with 600 kpc radius and 1.3 Mpc length, excluding the group emission. A similar, slightly larger, size (i.e. $\sim$ 800 kpc and 1.6 Mpc for radius and length, respectively) was also assumed by Sugawara et al. (2017) in their modelling. Here, we assume a relatively similar radius ($\sim$ 660 kpc) and a length of about 2 Mpc, which corresponds to the region outside the R_{200} of both GC1 and GC2, given their physical separation. In the simulated analog, none of the galaxy groups in the area lie between GC1 and GC2. This implies that the gas selected in the interconnecting region is mostly warm and diffuse, except for a minor fraction of colder gas located in galaxy-size haloes (see Sec. 4.2). The transition between outer cluster halos and pure inter-cluster gas is however difficult to determine. In our definition, gas and subhaloes in the clusters' periphery ($R_{200} < r < R_{\rm vir}$) are in fact comprised within the geometrical boundaries of the bridge (see Sec. 3.1.1). The presence of clumps in the far outskirts of clusters has been investigated recently in cosmological simulations by Angelinelli et al. (2021), finding that clumps around (and beyond) $\sim 3 \times R_{500}$ can be used to locate filaments connected to clusters, and to study the thermodynamics of diffuse baryons before they are processed by the interaction with the ICM of the host cluster. A moderate ($\lesssim$ 10% in mass) presence of dense halo gas associated to galaxies in short filaments is also found by Galárraga-Espinosa et al. (2020b), who investigated the properties of filaments in different cosmological simulations, including the Magneticum set.

From the analysis done on the selected pair, and given its geometrical configuration, we conclude that the majority of the bridge gas has not been stripped from the member clusters due to their interaction. The two clusters GC1 and GC2 are in fact separated by a physical distance that is $\sim 3 \times (R^1_{500} + R^2_{500})$ and their virial boundaries ($R_{\rm vir}$) do not overlap. The GC1 and GC2 spheres of influence ($\sim 3 \times R_{200}$), instead, are already overlapping and the two clusters are moving towards each other, as confirmed by the evolution shown in Fig. 4. We can expect they will finally merge. Observationally, it is more difficult to determine the physical distance of the A3391/95 components along the l.o.s. In this respect, the indications of some cold gas component in the interconnecting bridge (Reiprich et al. 2021) can still be consistent with a scenario similar to the simulated case. Namely, the filament has been forming in time during the LSS assembly and the two clusters can be in a pre-merging phase, in which no stripping nor direct interaction between the cluster's atmospheres has happened yet. A longer interconnecting bridge of pure-filament gas along the l.o.s., in case of a larger physical separation, could be observationally confirmed by the presence of colder ($T < 1$ keV) WHIM gas in a detailed spectral analysis of the bridge region.

An early interaction phase of the two pair members was instead found in Planck Collaboration et al. (2013), for a similar simulated system resembling A399–A401, with a significant part of the bridge gas stripped from the two clusters. The main difference, with respect to the A3391/95-like system considered here, was the 3D distance of the two clusters relative to their size. In that case, the two clusters (more massive than GC1 and GC2) were separated by a smaller physical distance relative to their size, with the two virial radii overlapping in all projections.

Despite the several similarities between the simulated system and the observed A3391/95, we finally note that none of the

groups found in the surroundings of the selected pair at $z = 0.07$ matches *exactly* the properties of the observed Northern Clump. Nonetheless, by selecting two interesting candidates we could investigate the expected signatures of infall towards the overdense Cosmic Web knot where the pair is located. The groups A and B serve as extreme limits, both with similarities and differences with respect to the real Northern Clump. Group A is an isolated massive group moving along with the main northern filament towards the pair system, like the Northern Clump, but is located at a too large distance to experience the direct influence of any of the main clusters. Group B, instead, is a smaller group outside of the main north-south filament and is already merging with one of the clusters. Group B, however, showed a configuration similar to the Northern Clump about ~ 3 Gyr ago ($z \sim 0.25$), when it was at a distance of $\sim 3 \times R_{200}$ from GC1. We use this example to speculate that the features presented by the Northern Clump in the *eROSITA* observations are consistent with a radial motion of the system towards A3391 and the pair (Veronica et al., submitted). Indeed, from the evolution of the group B between $z \sim 0.25$ and the final snapshot ($z = 0.07$), we observe slowing down of the gas compared to DM, and stripping of the gas in the later merging stages ($z \lesssim 0.16$), when the group B finally enters the virial boundary of GC1.

6. Summary and conclusions

We present results from the Magneticum cosmological hydrodynamical simulations on a case study resembling the binary cluster system in the observed *eROSITA* A3391/95 field. By investigating a cosmological comoving volume of $(352\,h^{-1}\,\mathrm{cMpc})^3$ at high resolution, we consider all possible close pairs of cluster-size haloes and select a candidate at $z = 0.07$ presenting several global similarities with the observed A3391/95 system. Specifically, by restricting to all clusters with $M_{500} > 10^{14}\mathrm{M}_\odot$ in the local Universe, we expect to find 300–400 pairs with physical separation smaller than 10 Mpc per $(\mathrm{Gpc})^3$. This is confirmed when larger cosmological volumes of the Magneticum suite are inspected. For our study, we focus in particular on the large-scale region of $20\,h^{-1}$ cMpc per side around the pair, approximating a physical size of ~ 26 Mpc for the given redshift and cosmology. The selected simulated system is located in a node of the cosmic web which is assembling, with filaments building up in time and substructures moving along with them towards the cluster pair. The main clusters in the pair are slightly less massive than the members of the observed A3391/95 system, despite a roughly similar mass ratio (M1/M2 $\sim$ 1.2) and configuration. The projected distance between the pair clusters is indeed similar (2.6 Mpc in the reference projection), with the regions enclosed by $3 \times R_{200}$ overlapping. The simulated system is in fact one of the ~ 7 close pairs found at $z = 0.07$, with member masses of $1.5 < M^{1,2}_{500}[10^{14}\mathrm{M}_\odot] < 3.5$ and a three-dimensional separation of $d_{3\mathrm{D}} \sim 4.5$ Mpc. Typically, our simulations predict in fact to find roughly $\sim$ 25 close ($d_{3\mathrm{D}} \lesssim 10$ Mpc) pairs per $(\mathrm{Gpc})^3$, whose members have masses in that range and mass ratio of M1/M2 $\lesssim 1.2$.

Given the encouraging similarity to the A3391/95 system in the *eROSITA* field, we then explored the properties and origin of the pair, and of the diffuse gas selected at $z = 0.07$ in different thermal phases and spatial regions. In the following we summarize the main results obtained from this study.

- The gas located in the pair bridge originates from distances of few-to-ten comoving megaparsecs away with respect to its final position. Furthermore, its accretion trajectories are almost perpendicular to the filamentary directions through which the gas found within the main clusters has been accreted, marking a distinctly different origin;
- Most ($\sim$ 90%) of the gas in the bridge was never inside the R_{200} radius of either cluster progenitor, and a substantial fraction ($\gtrsim$ 80%) was always beyond $2 \times R_{200}$ at $z \gtrsim 0.25$. The simulation study thus predicts that *the majority* of the bridge gas has not been stripped from the member clusters despite their closeness;
- The bridge gas is characterised by a typical temperature of $\sim$ 1 keV and overdensity around $\delta \lesssim 100$. Lower densities are expected at larger distances from the bridge spine ($\gtrsim$ 1 Mpc), or in longer filaments, where the colder WHIM phase is expected to become more significant (Galárraga-Espinosa et al. 2020b);
- In the whole pair region, the enrichment level of the warm diffuse gas and WHIM is fairly homogeneous and lower than for the hot ICM in the clusters (by a factor of $\sim$ 2, for the iron abundance) or the cold-dense gas in galaxies and star-forming regions. Nonetheless, a highly-enriched component is present at $z \lesssim 2$ in all gas selections, and is mostly related to early enrichment within galaxies and star-formation sites. This component, roughly $\sim$ 10–20% of the gas mass depending on the specific selection, persists also in the bridge, within small clumps (galaxies) or in the diffuse form after being stripped from those haloes;
- Similarly to the A3391/95 field observed by *eROSITA*, in the simulation we also find additional group-size objects in the surroundings of the pair (see also Ramos-Ceja et al., in prep.), mostly aligned along a prominent north-south filament structure spanning about $\sim$ 26 Mpc ($20\,h^{-1}$ cMpc) in projection (Fig. 2–4). We identify in particular 5 groups in the mass range $M_{500} \sim 1.4$–$9.6 \times 10^{13}\,\mathrm{M}_\odot$ at $z = 0.07$.
- The additional systems, along with filaments, trace the assembly of the LSS around the overdense node where the pair is finally located. In fact, by inspecting the properties and trajectories of two group-size haloes in particular, groups A and B, we find clear signatures of their motion along with filaments towards the pair. In both cases we find a strong alignment of the halo bulk (gas and dark matter) velocity with the infall direction towards the pair. The farther and isolated group A is characterised by a visible sloshing of the gas component with respect to the DM one, while no significant mergers characterize its mass accretion history, except for accretion of gas and smaller clumps (galaxies) through the filament. This is marked by the oscillating evolution of gas and DM infall velocity components as well as by the center shift between halo center and gas center of mass.
- The smaller group B is identified as a substructure gravitationally bound to the pair cluster GC1 at redshift $z \lesssim 0.16$ and is located in its outskirts at $z = 0.07$. Tracing the trajectory of the group towards the pair we find evidences of the influence of the GC1 cluster. At a projected distance of about $3 \times R^1_{200}$ from GC1, around $z \sim 0.25$, the gas radial velocity starts to systematically decrease compared to the DM one. While entering the outer atmosphere of GC1 ($z \lesssim 0.16$) it undergoes gas stripping, as marked by the decrease of bound gas mass by a factor ~ 3. The configuration corresponding to 3 Gyr ago ($z \sim 0.25$) shares several similarities with the case of the real Northern Clump relative to A3391, supporting the picture of its actual infalling motion towards the A3391/95 system (see Veronica et al., submitted).

The *eROSITA* superior soft response and large FoV has allowed for the first direct detection of the faint X-ray emission

from the diffuse gas in the bridge and filaments connected to A3391/95, drawing a consistent picture of the LSS that well compares to theoretical predictions. Our conclusions from simulations further support that the geometrical configuration of the A3391/95 system, its pre-merger phase and physical separation, together with the large-scale structure of the field in which it is located, provide an optimal target for unveiling the elusive warm-hot gas that populates the Cosmic Web filaments and for characterising its physical properties.

The *eROSITA* all-sky survey mode will finally enable for a more statistical approach, by providing a significantly larger sample of candidate multiple cluster systems and gas emission filaments. Combined and compared to theoretical predictions from simulations, where samples of binary or multiple cluster systems in various configurations can be statistically investigated as well, this will greatly benefit the baryon census in the Universe, especially through the detailed characterization of the chemo-energetic properties of the diffuse pristine gas.

Acknowledgements. The authors would like to thank the anonymous referee for constructive comments and suggestions that contributed to improve and clarify the presentation of this work. VB kindly acknowledges A. Merloni for providing comments on the manuscript and inspiring discussions with U. Maio on cosmic gas chemistry. This research was funded by the Deutsche Forschungsgemeinschaft (DFG, German Research Foundation) — 415510302, and also partially supported by the Excellence Cluster ORIGINS, which is funded by the DFG under Germany's Excellence Strategy — EXC-2094-390783311. Part of this work has been funded by the Deutsche Forschungsgemeinschaft (DFG, German Research Foundation) – 450861021. The Magneticum Pathfinder simulations have been performed at the Leibniz-Rechenzentrum with CPU time assigned to the projects pr86re and pr83li. KD acknowledges support through the COMPLEX project from the European Research Council (ERC) under the European Union's Horizon 2020 research and innovation program grant agreement ERC-2019-AdG 860744. This work was supported in part by the Fund for the Promotion of Joint International Research, JSPS KAKENHI Grant Number 16KK0101. This work is based on data from eROSITA, the soft X-ray instrument aboard SRG, a joint Russian-German science mission supported by the Russian Space Agency (Roskosmos), in the interests of the Russian Academy of Sciences represented by its Space Research Institute (IKI), and the Deutsches Zentrum für Luft- und Raumfahrt (DLR). The SRG spacecraft was built by Lavochkin Association (NPOL) and its subcontractors, and is operated by NPOL with support from the Max Planck Institute for Extraterrestrial Physics (MPE). The development and construction of the eROSITA X-ray instrument was led by MPE, with contributions from the Dr. Karl Remeis Observatory Bamberg & ECAP (FAU Erlangen-Nuernberg), the University of Hamburg Observatory, the Leibniz Institute for Astrophysics Potsdam (AIP), and the Institute for Astronomy and Astrophysics of the University of Tübingen, with the support of DLR and the Max Planck Society. The Argelander Institute for Astronomy of the University of Bonn and the Ludwig Maximilians Universität Munich also participated in the science preparation for eROSITA.

References

Akamatsu, H., Fujita, Y., Akahori, T., et al. 2017, A&A, 606, A1
Alvarez, G. E., Randall, S. W., Bourdin, H., Jones, C., & Holley-Bockelmann, K. 2018, 858, 44
Anders, E. & Grevesse, N. 1989, Geochim. Cosmochim. Acta, 53, 197
Angelinelli, M., Ettori, S., Vazza, F., & Jones, T. W. 2021, arXiv e-prints, arXiv:2102.01096
Asplund, M., Grevesse, N., Sauval, A. J., & Scott, P. 2009, ARA&A, 47, 481
Beck, A. M., Murante, G., Arth, A., et al. 2016, MNRAS, 455, 2110
Biffi, V., Dolag, K., & Böhringer, H. 2013, MNRAS, 428, 1395
Biffi, V., Dolag, K., Böhringer, H., & Lemson, G. 2012, MNRAS, 420, 3545
Biffi, V., Dolag, K., & Merloni, A. 2018a, MNRAS, 481, 2213
Biffi, V., Mernier, F., & Medvedev, P. 2018b, Space Sci. Rev., 214, 123
Bond, J. R., Kofman, L., & Pogosyan, D. 1996, Nature, 380, 603
Bonjean, V., Aghanim, N., Salomé, P., Douspis, M., & Beelen, A. 2018, A&A, 609, A49
Botteon, A., Cassano, R., Eckert, D., et al. 2019, A&A, 630, A77
Bregman, J. N. 2007, ARA&A, 45, 221
Briel, U. G. & Henry, J. P. 1995, A&A, 302, L9
Brüggen, M., Reiprich, T. H., Bulbul, E., et al. 2021, A&A, 647, A3
Bulbul, E., Randall, S. W., Bayliss, M., et al. 2016, ApJ, 818, 131
Cen, R. & Ostriker, J. P. 1999, ApJ, 514, 1
Cen, R. & Ostriker, J. P. 2006, ApJ, 650, 560
Chabrier, G. 2003, PASP, 115, 763
Colberg, J. M., Krughoff, K. S., & Connolly, A. J. 2005, MNRAS, 359, 272
Connor, T., Kelson, D. D., Mulchaey, J., et al. 2018, ApJ, 867, 25
Connor, T., Zahedy, F. S., Chen, H.-W., et al. 2019, ApJ, 884, L20
Cui, W., Knebe, A., Libeskind, N. I., et al. 2019, MNRAS, 485, 2367
Cui, W., Knebe, A., Yepes, G., et al. 2018, MNRAS, 473, 68
Davé, R., Cen, R., Ostriker, J. P., et al. 2001, ApJ, 552, 473
Davis, M., Efstathiou, G., Frenk, C. S., & White, S. D. M. 1985, ApJ, 292, 371
de Graaff, A., Cai, Y.-C., Heymans, C., & Peacock, J. A. 2019, A&A, 624, A48
Di Matteo, T., Springel, V., & Hernquist, L. 2005, Nature, 433, 604
Dolag, K., Borgani, S., Murante, G., & Springel, V. 2009, MNRAS, 399, 497
Dolag, K., Meneghetti, M., Moscardini, L., Rasia, E., & Bonaldi, A. 2006, MNRAS, 370, 656
Dolag, K., Mevius, E., & Remus, R.-S. 2017, Galaxies, 5, 35
Dolag, K., Vazza, F., Brunetti, G., & Tormen, G. 2005, MNRAS, 364, 753
Durret, F., Laganá, T. F., & Haider, M. 2011, A&A, 529, A38
Durret, F., Lima Neto, G. B., Forman, W. R., & Churazov, E. 2004, in Soft X-ray Emission from Clusters of Galaxies and Related Phenomena, ed. R. M. J. Lieu, Vol. 309, 53
Eckert, D., Jauzac, M., Shan, H., et al. 2015, Nature, 528, 105
Eke, V. R., Cole, S., & Frenk, C. S. 1996, MNRAS, 282, 263
Fabjan, D., Borgani, S., Tornatore, L., et al. 2010, MNRAS, 401, 1670
Finoguenov, A., Briel, U. G., & Henry, J. P. 2003, A&A, 410, 777
Fujita, Y., Tawa, N., Hayashida, K., et al. 2008, PASJ, 60, S343
Fukugita, M., Hogan, C. J., & Peebles, P. J. E. 1998, ApJ, 503, 518
Galárraga-Espinosa, D., Aghanim, N., Langer, M., Gouin, C., & Malavasi, N. 2020a, A&A, 641, A173
Galárraga-Espinosa, D., Aghanim, N., Langer, M., & Tanimura, H. 2020b, arXiv e-prints, arXiv:2010.15139
Gheller, C., Vazza, F., Brüggen, M., et al. 2016, MNRAS, 462, 448
Gheller, C., Vazza, F., Favre, J., & Brüggen, M. 2015, MNRAS, 453, 1164
Ghirardini, V., Bulbul, E., Hoang, D. N., et al. 2020, arXiv e-prints, arXiv:2012.11607
Gupta, N., Saro, A., Mohr, J. J., Dolag, K., & Liu, J. 2017, MNRAS, 469, 3069
Haardt, F. & Madau, P. 2001, in Clusters of Galaxies and the High Redshift Universe Observed in X-rays, ed. D. M. Neumann & J. T. V. Tran, 64
Hattori, S., Ota, N., Zhang, Y.-Y., Akamatsu, H., & Finoguenov, A. 2017, PASJ, 69, 39
Hirschmann, M., Dolag, K., Saro, A., et al. 2014, MNRAS, 442, 2304
Khabibullin, I. & Churazov, E. 2019, MNRAS, 482, 4972
Komatsu, E., Smith, K. M., Dunkley, J., et al. 2011, ApJS, 192, 18
Kovács, O. E., Bogdán, Á., Smith, R. K., Kraft, R. P., & Forman, W. R. 2019, ApJ, 872, 83
Libeskind, N. I., van de Weygaert, R., Cautun, M., et al. 2018, MNRAS, 473, 1195
Lim, S. H., Mo, H. J., Wang, H., & Yang, X. 2020, ApJ, 889, 48
Malavasi, N., Aghanim, N., Douspis, M., Tanimura, H., & Bonjean, V. 2020, A&A, 642, A19
Martizzi, D., Vogelsberger, M., Artale, M. C., et al. 2019, MNRAS, 486, 3766
Mazzotta, P., Rasia, E., Moscardini, L., & Tormen, G. 2004, MNRAS, 354, 10
Merloni, A., Predehl, P., Becker, W., et al. 2012, arXiv e-prints, arXiv:1209.3114
Mernier, F., Biffi, V., Yamaguchi, H., et al. 2018, Space Sci. Rev., 214, 129
Mitsuishi, I., Gupta, A., Yamasaki, N. Y., et al. 2012, PASJ, 64, 18
Nevalainen, J., Tempel, E., Ahoranta, J., et al. 2019, A&A, 621, A88
Nevalainen, J., Tempel, E., Liivamägi, L. J., et al. 2015, A&A, 583, A142
Nicastro, F., Kaastra, J., Krongold, Y., et al. 2018, Nature, 558, 406
Nicastro, F., Mathur, S., & Elvis, M. 2008, Science, 319, 55
Padovani, P. & Matteucci, F. 1993, ApJ, 416, 26
Parekh, V., Durret, F., Padmanabh, P., & Pandge, M. B. 2017, MNRAS, 470, 3742
Péroux, C. & Howk, J. C. 2020, ARA&A, 58, 363
Persic, M. & Salucci, P. 1992, MNRAS, 258, 14P
Piffaretti, R., Arnaud, M., Pratt, G. W., Pointecouteau, E., & Melin, J. B. 2011, A&A, 534, A109
Planck Collaboration, Ade, P. A. R., Aghanim, N., et al. 2013, A&A, 550, A134
Predehl, P., Andritschke, R., Arefiev, V., et al. 2020, A&A, accepted
Ragagnin, A., Dolag, K., Biffi, V., et al. 2017, Astronomy and Computing, 20, 52
Reiprich, T. H. & Böhringer, H. 2002, ApJ, 567, 716
Reiprich, T. H., Veronica, A., Pacaud, F., et al. 2021, A&A, 647, A2
Remus, R.-S., Dolag, K., Naab, T., et al. 2017, MNRAS, 464, 3742
Remus, R.-S. & Forbes, D. A. 2021, arXiv e-prints, arXiv:2101.12216
Sakelliou, I. & Ponman, T. J. 2004, MNRAS, 351, 1439
Schulze, F., Remus, R.-S., Dolag, K., et al. 2018, MNRAS, 480, 4636
Springel, V. 2005, MNRAS, 364, 1105
Springel, V., Di Matteo, T., & Hernquist, L. 2005, MNRAS, 361, 776
Springel, V. & Hernquist, L. 2003, MNRAS, 339, 289

Springel, V., White, S. D. M., Tormen, G., & Kauffmann, G. 2001, MNRAS, 328, 726
Steinborn, L. K., Dolag, K., Comerford, J. M., et al. 2016, MNRAS, 458, 1013
Sugawara, Y., Takizawa, M., Itahana, M., et al. 2017, PASJ, 69, 93
Tanimura, H., Aghanim, N., Bonjean, V., Malavasi, N., & Douspis, M. 2020a, A&A, 637, A41
Tanimura, H., Aghanim, N., Kolodzig, A., Douspis, M., & Malavasi, N. 2020b, A&A, 643, L2
Teklu, A. F., Remus, R.-S., Dolag, K., & Burkert, A. 2017, MNRAS, 472, 4769
Tempel, E., Stoica, R. S., Martínez, V. J., et al. 2014, MNRAS, 438, 3465
Thielemann, F.-K., Argast, D., Brachwitz, F., et al. 2003, in From Twilight to Highlight: The Physics of Supernovae, ed. W. Hillebrandt & B. Leibundgut, 331
Tittley, E. R. & Henriksen, M. 2001, ApJ, 563, 673
Tornatore, L., Borgani, S., Dolag, K., & Matteucci, F. 2007, MNRAS, 382, 1050
Tornatore, L., Borgani, S., Matteucci, F., Recchi, S., & Tozzi, P. 2004, MNRAS, 349, L19
Tuominen, T., Nevalainen, J., Tempel, E., et al. 2020, arXiv e-prints, arXiv:2012.09203
Ursino, E., Galeazzi, M., Gupta, A., et al. 2015, ApJ, 806, 211
Ursino, E., Galeazzi, M., & Roncarelli, M. 2010, ApJ, 721, 46
van den Hoek, L. B. & Groenewegen, M. A. T. 1997, A&AS, 123, 305
Vikhlinin, A., Burenin, R. A., Ebeling, H., et al. 2009, ApJ, 692, 1033
Werner, N., Finoguenov, A., Kaastra, J. S., et al. 2008, A&A, 482, L29
Wiersma, R. P. C., Schaye, J., & Smith, B. D. 2009, MNRAS, 393, 99
Woosley, S. E. & Weaver, T. A. 1995, ApJS, 101, 181

Table A.1: Number of pairs in the Magneticum Simulation cosmological volume Box2/hr at $z = 0.07$, for different selection criteria based on the pair members three-dimensional (3D) and projected (2D) distance and mass-ratios.

	$d_{3D} < 10$ Mpc	$d_{3D} < 15$ Mpc	$d_{3D} < 20$ Mpc	$d_{2D} < 5$ Mpc	$d_{2D} < 10$ Mpc
$M_{500}^{1,2} > 10^{14}\,M_\odot$					
any M1/M2	40	88	146	135	535
M1/M2 < 2	26	55	97		
M1/M2 < 1.5	19	42	78		
M1/M2 < 1.2	13	27	51		
$1.5 < M_{500}^{1,2}\,[10^{14}\,M_\odot] < 3.5$					
any M1/M2	8	15	25	27	82
M1/M2 < 2	8	15	24		
M1/M2 < 1.5	8	15	24		
M1/M2 < 1.2	7	11	19		

Notes. The 2D distance d_{2D} is considering any projection out of the three main Cartesian directions, namely we report the number of pairs for which the projected distance on at least one of the projection planes is < 5(10) Mpc (i.e. $d_{xy} < 5(10)$ Mpc $\vee$ $d_{xz} < 5(10)$ Mpc $\vee$ $d_{yz} < 5(10)$ Mpc).

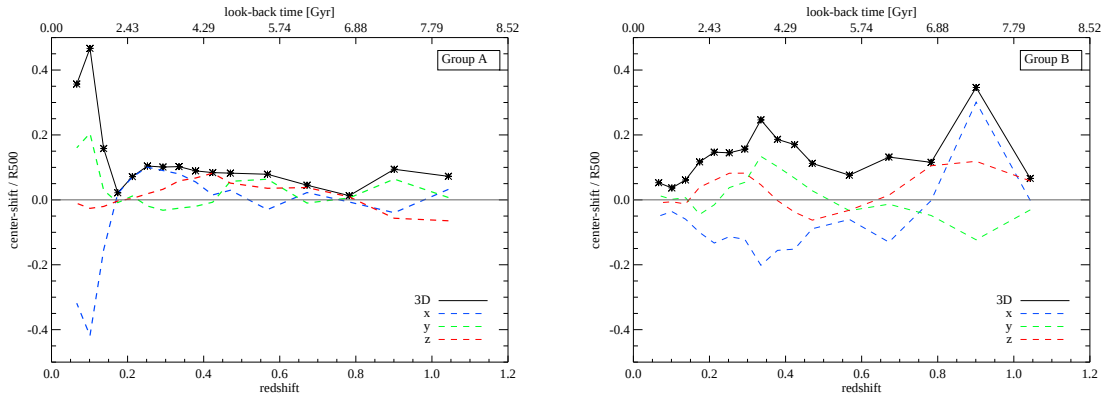

Fig. B.1: Redshift evolution of the center shift between the (bound) gas center of mass and the halo center, in units of R_{500}, for the groups A (left) and B (right) analysed in Sec. 4.4. We report the modulus and each separate component, as in the legend.

Appendix A: Appendix – Cluster pairs in the Magneticum Simulations

In Table A.1, we report the number of cluster pairs found in the Magneticum simulation (Box2/hr) at $z = 0.07$, for different separations and mass ratios[7]. We consider unique pairs of clusters with $M_{500}^{1,2} > 10^{14}\,M_\odot$ (448 haloes, uper half in the Table), as well as pairs where both haloes have masses in the range $1.5 < M_{500}^{1,2}\,[10^{14}\,M_\odot] < 3.5$ (165 haloes; lower half of the Table).

Appendix B: Appendix – Gas sloshing in groups A and B

In Fig. B.1 we report the center-shift evolution for the groups A (left) and B (right) discussed in Sec. 4.4. The center-shift is computed as the three-dimensional difference between the center of the halo potential well (defined as the position of the most-bound particle) and the bound-gas center of mass, and is given in units of the halo R_{500} radius, at any given redshift between $z \sim 1$ and $z \sim 0.07$. In addition to the modulus of the shift, we also show the three components along the major simulation axes, separately (as in the legend). Comparing the two panels, we note that the amplitude of the shift is overall larger in the smaller infalling group B, relative to its size. Considering the separate shift components, an oscillating opposite trend in the *xy* plane is observed in both cases, which indicates a sloshing feature of the gas component relative to the DM.

Appendix C: Appendix – Metallicity distribution

In Fig. C.1 we show the distributions of iron abundance and O/Fe abundance ratio, for the hot gas ($T > 10^7$K) and WHIM ($10^5 < T$[K] $< 10^7$ and $\delta < 100$) in the $(7\,h^{-1}\,\mathrm{cMpc})^3$ region around the selected pair (see Sec. 4.2). Gas particles in the two cases are selected at $z = 0.07$ and tracked back in time. By comparison with Fig. 11, we notice that the hot and WHIM gas present overall similar trends to the hot ICM in clusters and the bridge gas, respectively — as discussed in Secs. 4.2–4.3. Furthermore, the mass fraction distribution of the iron abundance is reported (left-most panels) to demonstrate that the normalization of the distributions

[7] In order to compute the mass ratio M1/M2, we consider M_{500}.

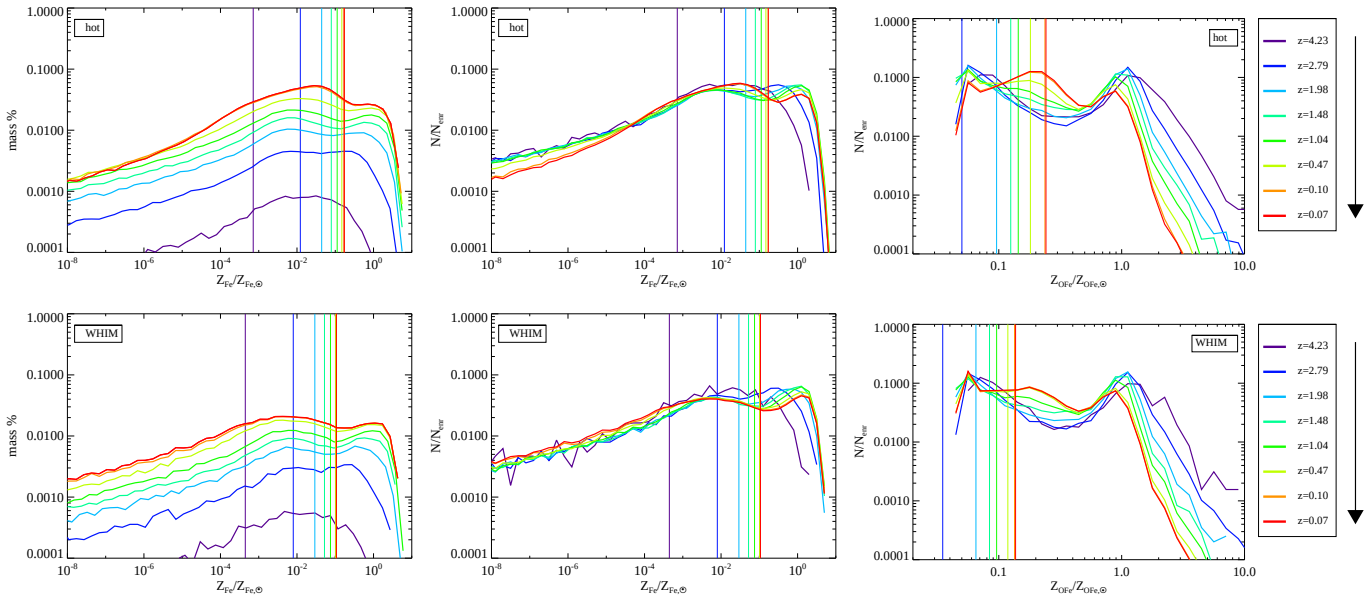

Fig. C.1: Iron abundance and O/Fe ratio distribution for the hot gas and WHIM (upper and lower rows, respectively), for different redshifts as in the legend. Displayed in the left-hand-side panels for comparison, the mass fraction distribution of the hot-gas iron abundance. At each redshift, the mass fractions are normalized to the total gas mass of the selected subsample.

for a given gas selection indeed increases with time, indicating as expected that the mass fraction of the enriched gas grows from high to low redshift (as in Fig. 12).